Award DE-EE0011264, Deliverable D.2.1, Resource Characterization Report, OPALCO site in Rosario Strait, WA (USA)

Jim Thomson, Chris Bassett, Brian Polagye
Applied Physics Lab., Univ. of Washington

March 20, 2025

Contents

1 Introduction **4**

2 Methods **4**
2.1 Mobile survey 4
2.2 Stationary measurements 5
2.3 Modeled Turbine Performance 8

3 Results **10**
3.1 Mobile survey 10
3.2 Stationary measurements 10
3.2.1 Sea Spider tripod 10
3.2.2 Stablemoor 14
3.2.3 Surface Buoy 17
3.3 Annual Energy Production (AEP) and Capacity Factor (CF) estimates 18
3.4 Surface Waves 18
3.5 Ambient sound levels 19
3.6 Stratification 24
3.7 Fish tags and porpoise clicks 24

4 Discussion **26**

5 Conclusion **26**

6 Data and software archive **26**

7 Acknowledgments **26**

A Quality control / assurance of Sea Spider tripod data **29**

B Quality control / assurance of Stablemoor data **33**

C Quality control / assurance of Surface Buoy data **39**

D Tidal Harmonic Analysis **41**

E Additional calculations for FERC application **43**

List of Figures

1 Site map. . . . 4
2 Stationary platforms. . . . 5
3 Deployment geometry. . . . 7
4 Mobile ADCP survey results. . . . 10
5 Sea Spider tripod Sig250 profiles of horizontal speed. . . . 11
6 Sea Spider tripod Sig250 horizontal components. . . . 12
7 Sea Spider tripod time-averaged profiles. . . . 12
8 Histograms of hub-depth speed and power production from Sea Spider tripod. . . . 13
9 Sea Spider Sig250 turbulence results. . . . 13
10 Horizontal speed measured by Stablemoor. . . . 14
11 Stablemoor Sig500 horizontal components. . . . 15
12 Stablemoor time-averaged profiles. . . . 15
13 Histograms of hub-depth speed and power production from the Stablemoor. . . . 16
14 Stablemoor turbulence results. . . . 16
15 Surface Buoy aquadopp results 17
16 Time series of surface wave heights and peak periods measured from the Stablemoor. . . . 18
17 Joint histogram of surface wave heights and peak periods measured from the Stablemoor. . . . 19
18 Ambient Sound Pressure Levels. . . . 20
19 Sound Pressure Levels and currents for 103 days. . . . 21
20 Sound Pressure Levels and currents for 1 day. . . . 22
21 PDFs of sound levels. . . . 23
22 Ambient sound spectra. . . . 23
23 Ambient Sound Pressure Level (SPL) statistics. . . . 24
24 Temperature versus salinity measured on the Stablemoor. . . . 25
25 CPOD detections by certainty level and click event type. . . . 25
A1 Sea Spider tripod Sig250 ancillary data. . . . 29
A2 Sea Spider tripod Sig250 backscatter amplitude. . . . 30
A3 Sea Spider tripod Sig250 Doppler correlations. . . . 31
A4 Sea Spider tripod Sig250 profiles of velocity components. . . . 32
A5 Sea Spider tripod Sig250 vertical velocity error estimates. . . . 33
B1 Stablemoor pitch and roll, heading, and water temperature. . . . 34
B2 Stablemoor merged Sig500s backscatter amplitude. . . . 35
B3 Stablemoor merged Sig500s Doppler correlation. . . . 36
B4 Stablemoor merged Sig500s velocity components. . . . 37
B5 Stablemoor merged Sig500s vertical velocity error estimates. . . . 38
C1 Surface buoy Aquadopp pith and roll, heading, and temperature. . . . 39
C2 Surface buoy Aquadopp amplitude. . . . 40
C3 Surface buoy Aquadopp velocity components, in beam coordinates. . . . 40
D1 Joint probability of velocity components from harmonic reconstruction (left, 1 year duration) and from observations (right, 103 days duration). . . . 41
D2 Exceedance probabilities for scalar current speed a hub depth. Results for 103 day observations (blue), 103 day reconstruction (green), and 1 yr reconstruction (magenta). . . . 42
E1 Time series of water depth (upper left) and current speed (lower left). Current speeds versus tidal stage (right). . . . 45

1 Introduction

This report presents a resource characterization of the tidal currents at a proposed site for power generation in Rosario Strait, WA (USA). Acoustic Doppler Current Profilers (ADCPs) were deployed to measured tidal currents, turbulence, and surface waves at the site. The measurements followed established technical specifications (IEC 62600-201) and were informed by previous work at other tidal power sites in the region. All work was completed from the Research Vessel (R/V) Jack Robertson, which is owned and operated by Applied Physics Laboratory, University of Washington (APL-UW).

The site is centered just east of Blakely Island on the western edge of Rosario Strait at 48.56114 °N, -122.76792 °W. As shown in Figure 1, the site is north of the fixed navigation light at Black Rock and north of the G-11 buoy. The site was selected based on the results of the FVCOM numerical circulation model from Pacific Northwest National Laboratory (PNNL), as detailed in Calandra et al. [2023]. That modeling study noted that the tidal resource is highly localized near Blakely Island, where the currents are much stronger (up to 3.6 m/s) than in the center of the Rosario Strait. The only known prior measurements are from NOAA current survey station PUG 173 in 2019 toward the middle of the channel, and from an APL-UW collaboration with NREL in 2017 at eastern edge of Rosario Strait [McVey et al., 2025].

Water depths are 80-95 m at the site. There is steep bathymetry close to Blakely Island, and this resource characterization study included a stand-off distance of 100 m from the shore. This was both for the safety of the vessel and to ensure room for the moorings of the proposed Orbital Marine Power 'O2' turbine. The O2 turbine is surface-deployed and therefore resource characterization focuses on the upper portion of the water column.

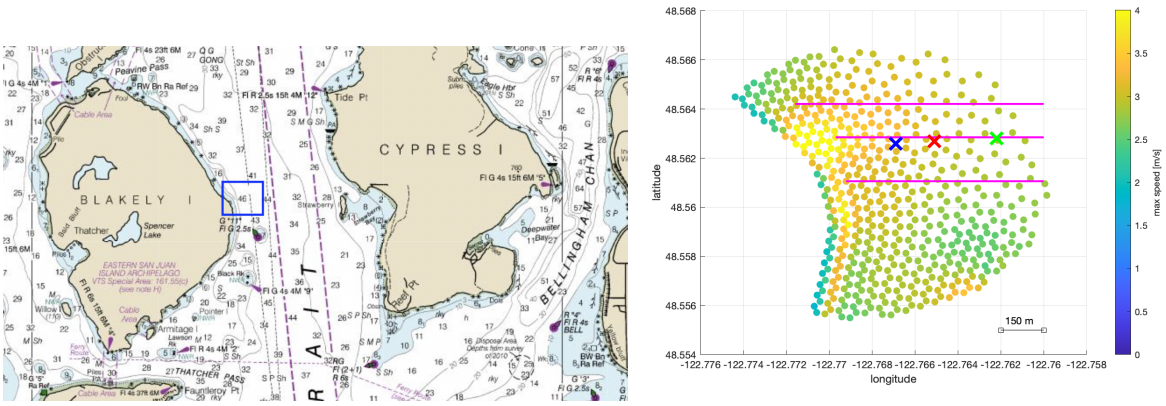

Figure 1: Left: NOAA chart of Rosario Strait (WA, USA) with depth in fathoms and OPALCO tidal site outlined in blue box. Right: maximum current speeds predicted by PNNL FVCOM model within the site. Magenta lines are mobile survey grid, and X's are stationary measurement platforms.

2 Methods

The site survey consisted of spatially-resolved, mobile measurements collected from R/V Robertson and temporally-resolved, stationary measurements from three platforms. The use of multiple platforms for the stationary measurements mitigated some of the risks in data collection, while also increasing spatial coverage.

2.1 Mobile survey

The mobile survey was conducted on 1 Oct 2024 with a down-looking RDI 300 kHz ADCP mounted beneath the R/V Robertson. This information was used to make the final selection of points for the stationary ADCP

deployments. The mobile survey followed three east-west lines (Figure 3), which were repeated 7 times (i.e., 7 laps) during the morning ebb tide and 5 times (i.e., 5 laps) during the afternoon flood tide. The ADCP was set to ping continuously at 2 Hz, with bottom tracking enabled as the preferred reference velocity (to convert observed currents to the fixed-earth reference frame). A bin size of 5 m was selected to reduce Doppler noise [Brumley et al., 1991], and ensembles of 30 seconds duration were mapped to gridded positions to produce current maps for each phase of the tide. These data were also used to create pseudo-time series at each prospective mooring site, following the methods of Palodichuk et al. [2013].

2.2 Stationary measurements

Stationary measurements of tidal currents were collected from 2 Oct 2024 to 13 Jan 2025 (total duration: 103 days). This duration is sufficient to determine at least 20 tidal constituents using classic tidal harmonic analysis [Pawlowicz et al., 2002], and it is also sufficient to determine a purely statistical description of the tidal currents [Polagye and Thomson, 2013]. The analysis that follows emphasizes the statistical approach, while also including the harmonic analysis.

The measurements used ADCPs on three different platforms: a Sea Spider seafloor tripod (SS), a stablemoor (STBM) subsurface mooring, and a surface buoy (SB) mooring. The sea spider tripod measurements alone are sufficient for resource characterization. The additional measurements were included for risk mitigation, spatial context, and informing future revisions to IEC 62600-201.

Figure 2: Sea Spider seafloor tripod and Stablemoor sub-surface buoy just before deployment. The shoreline of Blakely Island at the end of survey line 3 is just behind the vessel (100 m stand-off distance).

The Sea Spider (SS) is a fiberglass sea floor tripod. It has 272 Kg of lead ballast distributed at three feet, plus another 91 Kg on the frame. This platform has been used extensively at the nearby Admiralty Inlet, where the ballast was sufficient to maintain position in a rock/cobble seabed with currents up to 4 m/s [Thomson et al., 2012, Polagye and Thomson, 2013, Guerra and Thomson, 2017]. An up-looking Nortek Signature 250 ADCP made full-depth profiles of the tidal currents. The Sea Spider is bottom-mounted and thus has no watch circle. However, the beam angle of the Signature 250 is 20 deg, and this creates a cone with a 35 m radius at the surface in a water depth of 92 m. Tranformation of along-beam velocity components to geographic east-north-up components requires the assumption of homogeneous currents over this cone. Based on the mobile survey, this is reasonable assumption at the site. This type of seafloor mount is ideal for resource characterization; however, it requires a lower frequency ADCP (250 kHZ) to span the full depth (92 m). The use of a lower frequency increases Doppler noise in the measurements (when maintaining the 1 m bin size required in IEC 62600-201) and usually precludes the measurement of surface waves. The Sea Spider also provided a platform of opportunity for ancillary environmental measurements. Specifically,

hydrophones, a porpoise click detector, and fish tag receiver were deployed alongside the Sig250 ADCP.

The Stablemoor mooring (STBM) is a subsurface platform with a streamlined shape designed to minimize drag. The Stablemoor was suspended in the middle of the water column, with a pair of down-looking and up-looking Nortek Signature 500 ADCPs. The mid-water location enabled the use of 500 kHz instruments with reduced Doppler noise (i.e., improved precision) relative to the 250 kHz on the Sea Spider. The up-looking Sig500 also provided surface wave measurements via acoustic surface tracking. The up- and down-looking Sig500 measurements are combined to form full-depth profiles of currents and turbulence. Stablemoor moorings have previously been used in strong tidal currents throughout Puget Sound [Harding et al., 2017, Kilcher et al., 2017] and Arctic environments [Brenner et al., 2021]. In strong currents, the mooring is pushed downward by drag forces (up to 15 m, in this deployment). This has a minimal effect on the measurements, because the Stablemoor remains trim and level during mooring blow-down, and results in a mooring watch circle with a radius of 30 m. Combined with the 25 deg beam angle of the Sig500 producing an effective ADCP cone with 21 m radius, the total footprint of the stablemoor measurements is a radius of 51 m. The Stablemoor also provided a platform of opportunity for a Conductivity, Temperature, and Depth (CTD) sensor to characterize variations in temperature and salinity (and thereby infer stratification).

The Surface Buoy (SB) mooring was a tribal government requirement to provide a visual marker to help subsistence fisherman avoid entanglement with the nearby subsurface Stablemoor mooring. The surface buoy supported an additional down-looking ADCP (Nortek Aquadopp 1 MHz) to make opportunistic measurements near the surface. This filled a known gap in near-surface measurements from the other up-looking ADCPs, which have surface reflections that obscure velocities for $z > d\cos(\theta)$, where d is the depth of the water, θ is the angle of the beam relative to the vertical, and z is the distance above the seafloor [Lentz et al., 2022]. The SB mooring watch circle has a radius of 140 m.

The three stationary platforms were deployed from the R/V Robertson on 2 Oct 2024. The deployed locations were verified upon recovery on 13 Jan 2025, with horizontal accuracy of ±5 m. Figure 3 shows the layout of the stationary platforms.

Table 1: ADCP configurations

Platform	**ADCP kHz (look)**	**Bins**	**Profile, z**	**Ensembles**	$< \sigma_N >$	**Ping rate**	σ_N
Sea Spider	Sig 250 (up)	1 m	0 to 86 m	2 of 10 min	0.027 m/s	1 Hz	0.210 m/s
Stablemoor	Sig 500 (up)	1 m	45 to 82 m	2 of 10 min	0.010 m/s	1 Hz	0.073 m/s
Stablemoor	Sig 500 (down)	1 m	0 to 45 m	2 of 10 min	0.010 m/s	1 Hz	0.073 m/s
Surface buoy	AQD 1000 (down)	1 m	70 to 86 m	2 of 10 min	0.006 m/s	1 Hz	n/a
Robertson	WH 300 (down)	5 m	0 to 100 m	30 s	0.017 m/s	2 Hz	n/a

When using ADCP measurements to characterize tidal sites, IEC 62600-201 specifies a vertical resolution of 1 m (i.e., bin size), ensemble averages calculated over at least 2 minutes out of every 10 minutes, and ensemble precision $< \sigma_N >$ less than 0.05 m/s. Table 1 presents the ADCP configurations designed around these requirements, with the additional step of staggering the sampling to avoid cross-contamination of the acoustic signals between ADCPs in close proximity. The staggered approach limits the overall duty cycle of a single instrument, but still meets the required 2 minutes out of every 10 minutes.

It is well-known that single-ping velocity profiles have large uncertainties in velocity, sometimes referred to as Doppler noise. This is quantified with the standard deviation of velocity caused by noise, σ_N. For broadband Doppler systems, this can be calculated *a priori* from the acoustic frequency and the bin size [Brumley et al., 1991]. The values in the table come from the manufacturer software. Velocity uncertainty is reduced by creating ensemble averages of the data, denoted with brackets $<>$, for which the uncertainty is reduced by factor $1/\sqrt{2n}$, where n is the number of pings included in the ensemble. This study uses $n = 120$ for all stationary measurements.

Single-ping uncertainties σ_N can be large (especially when using 1 m bins on a 250 kHz ADCP), and this noise must be removed when estimating turbulence statistics. Following Thomson et al. [2012], the turbulent

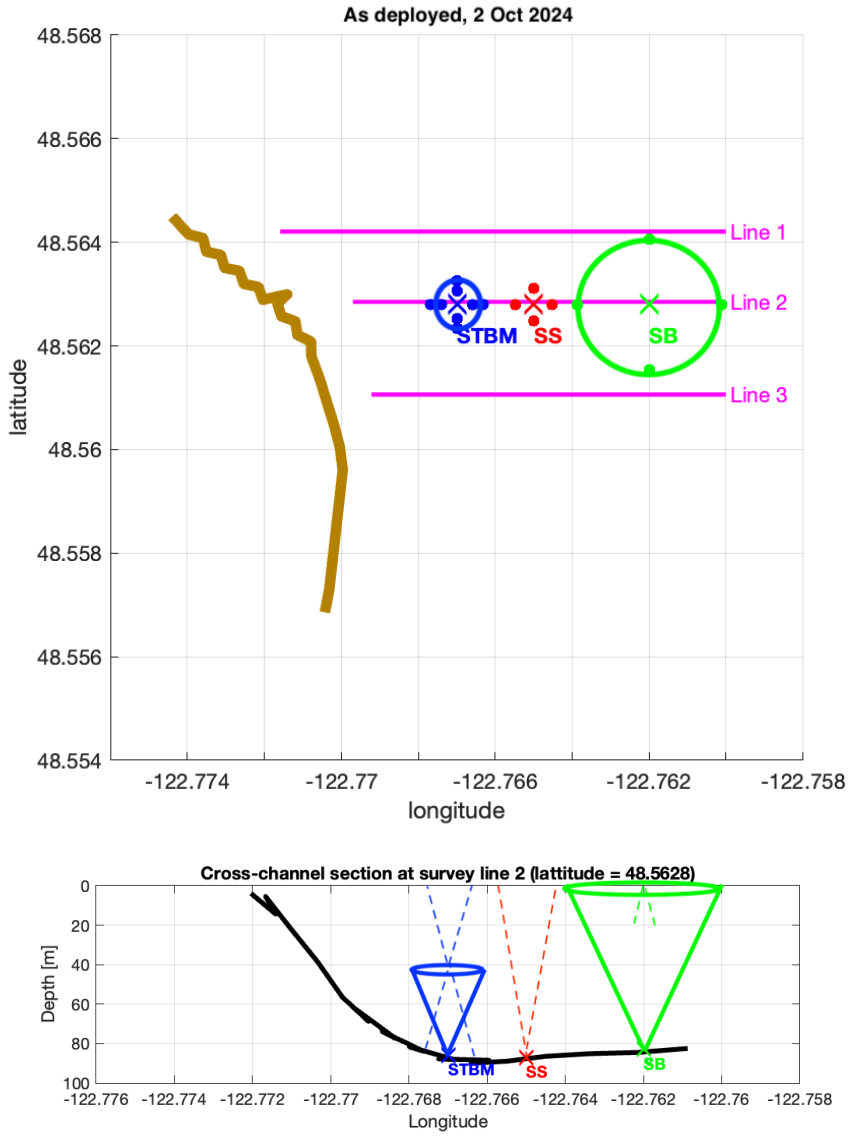

Figure 3: Plan view (top) and side view (bottom) of the stationary platforms, including watch circles (solid lines) and ADCP beam cones (dashed lines). The brown curve is the shoreline, and the black curve is teh seafloor.

intensity is calculated as

$$TI = \frac{\sqrt{\sigma_u^2 - \sigma_N^2}}{< U >}, \tag{1}$$

which assumes that the variance caused by Doppler noise is independent of the true turbulent fluctuations (i.e., no cross-terms in the variance). The standard deviation of the observed currents σ_u is calculated within each ensemble using a horizontal speed $U = \sqrt{u^2 + v^2}$. The full velocity components are determined from the five beams of each ADCP in a coordinate transform that returns eastward (u), northward (v), and upward (w).

Many other turbulence parameters can be estimated with single-ping ADCP data, including dissipation rate Wiles et al. [2006], shear [Bassett et al., 2013], turbulent spectra [Thomson et al., 2012], and Reynolds stresses [Guerra and Thomson, 2017]. These are omitted in this initial characterization, though they can be readily calculated from the collected data.

A relevant metric for tidal turbine performance is the kinetic power density incident on the rotor (i.e., the kinetic energy flux per unit rotor area)

$$\frac{P_{in}}{A} = \frac{1}{2}\rho U^3 \tag{2}$$

where ρ is the water density.

2.3 Modeled Turbine Performance

Polagye and Thomson [2013] defined a simple model for the power produced P by a turbine with three operating regimes as

$$\begin{aligned} P(t) &= 0, \quad U_{hub} < U_c \\ P(t) &= \frac{1}{2}\rho\pi R^2 U_{hub}^3 C_e, \quad U_c \leq U_{hub} \leq U_r \\ P(t) &= \frac{1}{2}\rho\pi R^2 U_r^3 C_e, \quad U_{hub} > U_r \end{aligned} \tag{3}$$

where U_c is the cut-in speed, U_r is the rated speed, C_p is an efficiency coefficient ("water-to-wire"), and R is the turbine radius.

The observed time series is used to estimate the Annual Energy Production (AEP) as

$$\text{AEP} = \frac{T_{\text{year}}}{T} \int_0^T P(t)\, dt, \tag{4}$$

where T is the duration of observations (103 days) and T_{year} is the length of a year in the same units. This assumes that the duration is sufficient to capture a representative statistic distribution of current speeds at the site, which is true for durations > 90 days at most tidal sites. This study uses $T = 103$ days and $dt = 10$ minutes, with the following representative values to approximate the Orbital Marine Power 'O2' turbine: $U_c = 0.7$ m / s, $U_r = 2.25$ m/s, $C_p = 0.39$, $R = 13.5$ m. These are the values for a single turbine; the 'O2' turbine actually has a pair of turbines, and thus the reported AEP values are doubled. The 'O2' turbine is designed to be deployed from the surface, with a hub depth $d_{hub} = R + 3.5$ m (i.e., the rotor tip is 3.5 m below the water surface at every stage of the tide).

Alternatively, tidal harmonic analysis of the observations can be used to determine amplitudes and phases of known tidal constituent frequencies, and then these can be used to estimate a full year of $P(t)$. This year-long predicted timeseries is then integrated to determine AEP without the $\frac{T_{\text{year}}}{T}$ factor in Eq. 4. The IEC 62600-201 specification is for harmonic analysis to resolve a minimum of 20 tidal constituents and demonstrate a reconstruction of the observations that captures at least 95% of the variance. This study uses v1.5b of the T-Tide software in Matlab [Pawlowicz et al., 2002] to resolve 35 constituents of the u, v tidal

currents (as complex-valued input to T-tide) and captures 96% of the variance. The details are included in an appendix.

A second performance metric is the capacity factor,

$$CF = \frac{\int_0^T P(t)dt}{TP_{rated}}, \tag{5}$$

which indicates how much the of the full capacity of the turbine is utilized. Here, the capacity factor is based on a rated power of $P_{rated} = 1.3MW$. For tidal sites, this number is often much lower than 0.5 (i.e., half capacity), because the natural tidal cycles have weak currents (slack) between each ebb and flood. In Puget Sound, capacity factors are further reduced by a diurnal inequality (i.e., two ebb and flood cycles per day, but of uneven strength).

3 Results

3.1 Mobile survey

Figure 4 shows the currents surveyed during the peak ebb and peak flood on 1 Oct 2024. The headland intensification predicted by the model is evident (larger arrows to the north of the headland than in the main channel on ebb), as is a strong back-eddy near shore (small arrows to the south of the headland on ebb). This region of separated flow causes an intense lateral shear that is prominent in section views (lower panels of Figure 4), where the currents change from 2 m/s to under 0.5 m/s within 100 m. This is also a region of intense turbulence, which was visually apparent from the deck of the vessel and noted repeatedly by the vessel operator.

The final choice of sites for the stationary measurements avoided this region of separated flow, both as a risk mitigation for the deployed platforms and as practical limit on the seabed slope feasible for deployments.

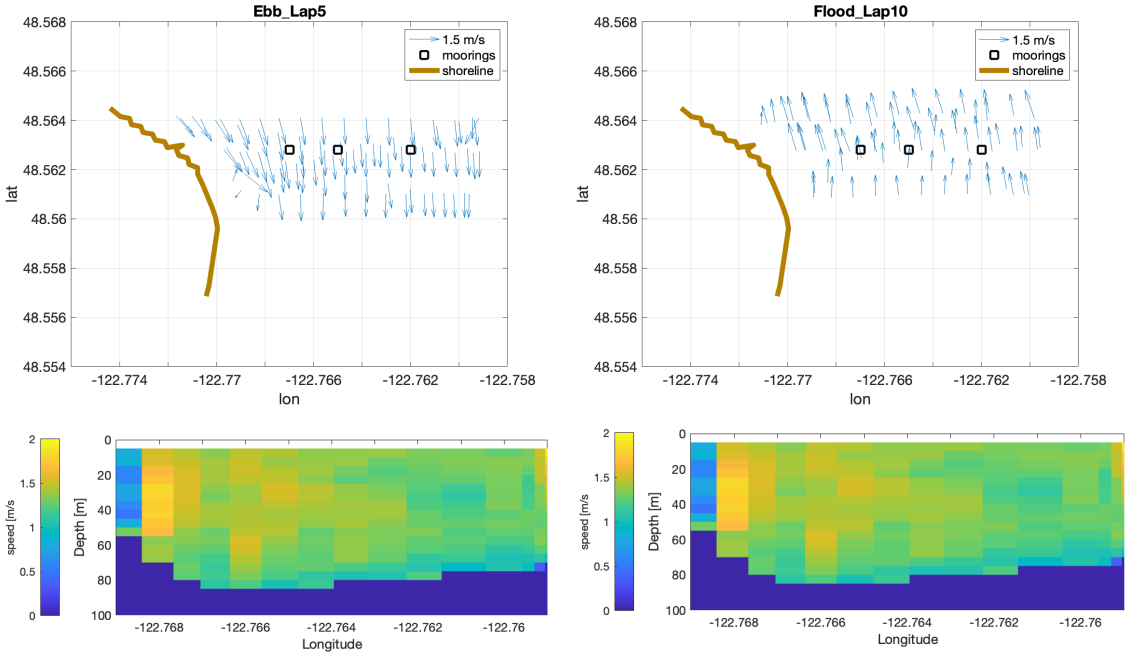

Figure 4: Maps of currents from mobile ADCP survey, with section views below.

3.2 Stationary measurements

The stationary measurements use a vertical coordinate z, which is meters above the local seafloor ($z = 0$ m) at the location of each platform. Where necessary, the depth d below the water surface is also used (e.g., to determine the hub-depth of the turbine). The z is fixed; the d is relative to the surface at each stage of the tide. All directions are reported relative to magnetic north, using coordinate transformations based on instrument magnetometers with factory calibrations. All data use UTC timestamps.

3.2.1 Sea Spider tripod

The Signature 250 on the Sea Spider platform provided extremely clean data and is most conventional; the results that follow emphasize these data. The quality qontrol and quality assurance checks are included as an appendix. The depth profiles of horizontal current speed are shown in Figure 5, along with the elevation of the water surface from the integrated pressure gauge. The maximum tidal elevation range is 4.0 m. The

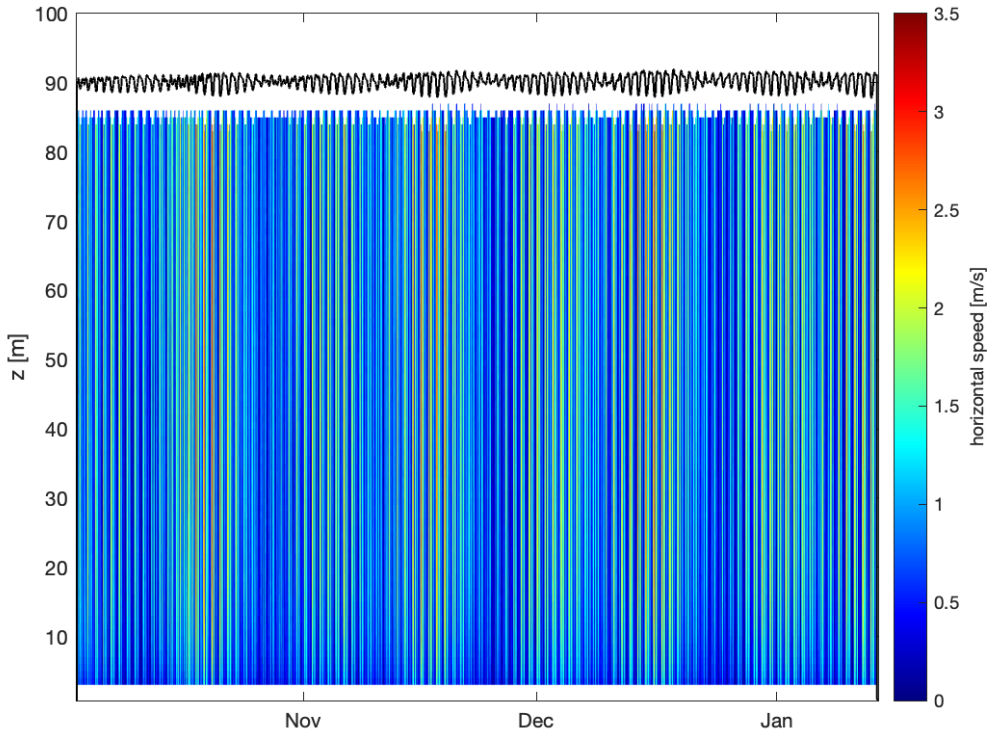

Figure 5: Sea Spider tripod Sig250 profiles of horizontal speed.

region of acoustic reflections near the surface was removed from the ADCP as part of the quality control. The data show the strong spring-neap cycle and diurnal inequality of the tides in the Pacific Northwest. The strongest tides are observed near the winter solstice, as expected.

The horizontal components are plotted together in Figure 6 to present the shape of the tidal ellipse and the principal axes of the flow. The flow veers slightly with depth, such that flows are aligned 305°Magnetic at the surface and 315°Magnetic near the seafloor. The ebbs (toward the southeast) are slightly stronger than the floods (toward the northwest). The increased scatter on the ebb is probably related to flow separation and eddy shedding from the headland.

The time-average vertical profiles are shown in Figure 7, along with horizontal lines to indicate turbine hub height and rotor sweep. The red areas are the data removed because of acoustic reflections from the surface. The speed and power profiles have familiar logarithmic (or power law) shapes, and the principal-axis profile has a modest amount of veering. The profiles indicate minimal velocity variation over the proposed rotor depth, and thus support the usage of a simple $U_{hub}(t)$ in Eq. 3 (as opposed to an integral of $U(t,z)$ over the turbine radius). Calandra et al. [2023] found this approximation to be accurate unless significant vertical shear is present, which typically only occurs for smaller rotors in closer proximity to the seabed.

The current speed at hub depth U_{hub} is determined for each ensemble by selecting the bin 17 m below the measured surface (from the depth given by the pressure sensor). A histogram of U_{hub} is shown in Figure 8, along with a histogram of the resulting power from the model turbine (Eq. 3). The velocity histogram is mostly smooth, with a shape that resembles a chi-squared distribution. The power histogram has an expected spike at the rated power of 1400 kW, because this value is repeated for any conditions with $U_{hub} \geq U_r$.

The single ping data from the Sig250 are used to calculate the turbulence statistics of the horizontal

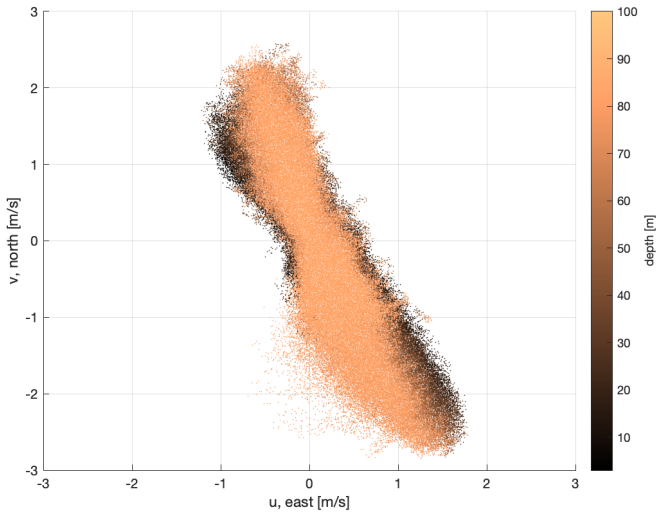

Figure 6: Sea Spider tripod Sig250 horizontal components and principal axes. Color is height of each bin above the seafloor, z.

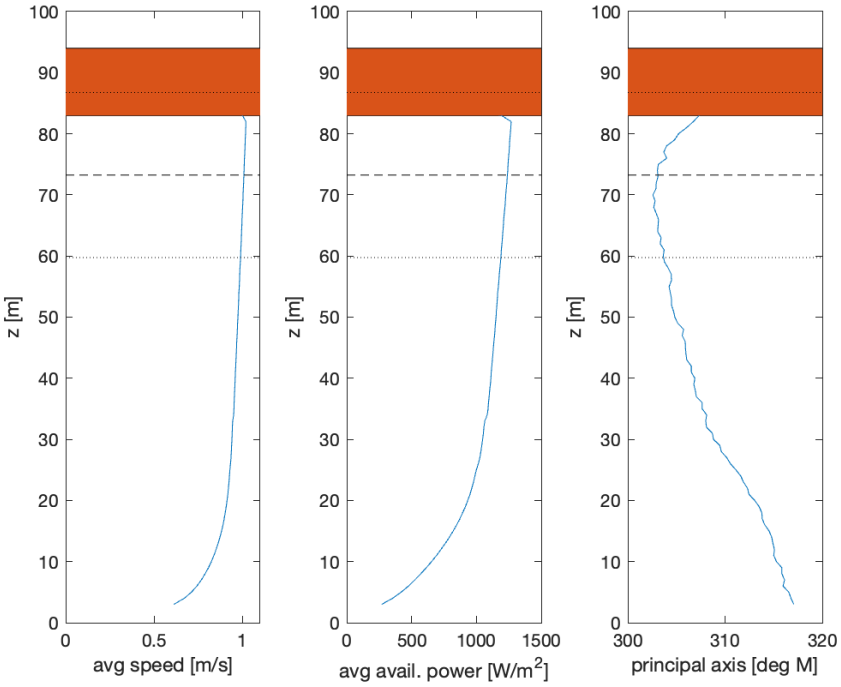

Figure 7: Sea Spider tripod Signature 250 profiles of average speed, available power density, and principal axes.

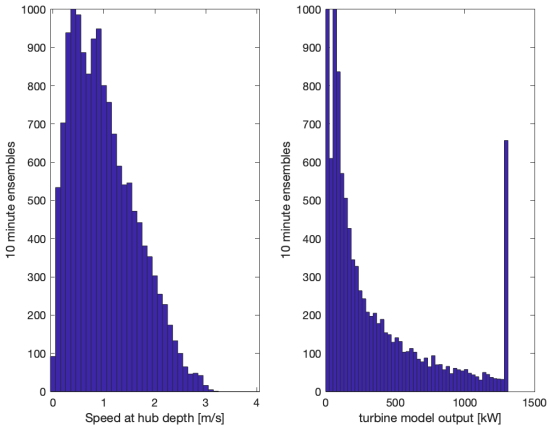

Figure 8: Histograms of hub-depth speed and power production from Sea Spider tripod.

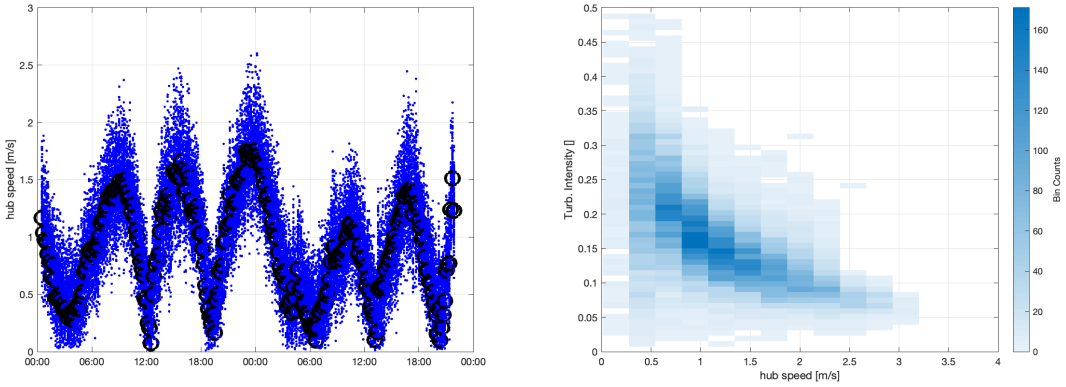

Figure 9: Sea Spider tripod Sig250 example raw time series (left) and turbulent intensity versus speed (right). The blue dots are single-ping data every 1 second, and the black circles are ensembles every 10 minutes.

speeds at hub depth for each ensemble (Eq. 1). Figure 9 shows an example 2-day time series with single-ping data and ensemble values, along with the TI results from the entire 103-day deployment as a function of hub speed. The TI results are consistent with many previous studies, in which TI converges to 10% at the higher inflow speeds. The data are of sufficient quality for determining other turbulence metrics, such as TKE spectra, dissipation rate, and Reynolds stresses, but these are left for a future stage of characterization.

3.2.2 Stablemoor

The Sig500s on the Stablemoor provided excellent data, with reduced Doppler noise σ_N achieved at the expense of slight motion contamination from the mooring. Figure 10 shows the scalar speed profiles from the up- and down-looking Sig500s merged into a single dataset. The profiles shift up and down with the tide, and with the mooring 'blow-down' caused by drag. This can create artifacts (sampling bias) when averaging in fixed height bins z, but only for bins that periodically lack data near the surface. This does not affect the portion of each profile relevant to the turbine. A gridded product is also included in the MHKDR data submission (which looks similar).

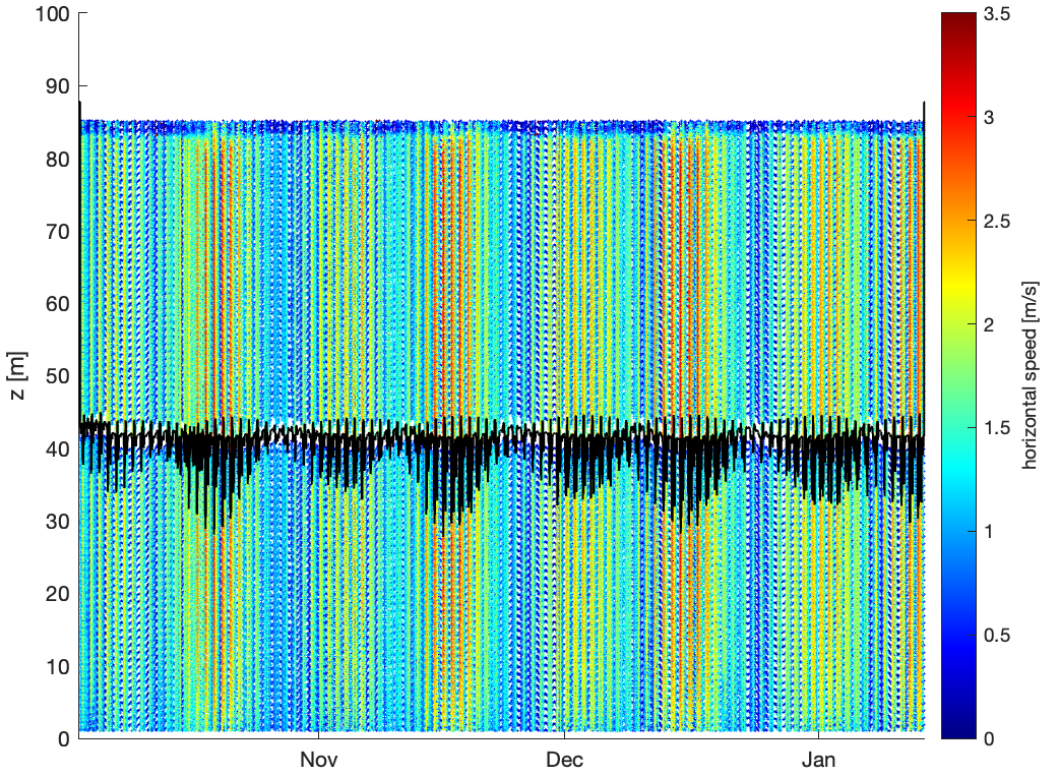

Figure 10: Horizontal speed measured by the Signature 500s on the Stablemoor. The black curve shows the depth of the Stablemoor, which decreases during strong flows.

Figure 11 shows the horizontal components of velocity measured by the Stablemoor, which have a principal axis that is similar to the measurements from the Sea Spider. There is more scatter in the Stablemoor measurements, which probably the result of lingering platform motion and possibly the result of large eddies shed close to the shore. The Stablemoor was the closest platform to the back-eddy and, so, potentially more affected.

Figure 12 shows the average profiles of speed, power, and principal axes measured by the Stablemoor. These are again similar to the Sea Spider measurements, with almost constant values over the depth range of the proposed O2 turbine (dashed lines). The red regions should the data with surface reflections that was removed during quality control.

The current speed at hub depth U_{hub} is determined for each Stablemoor ensemble by selecting the bin 17

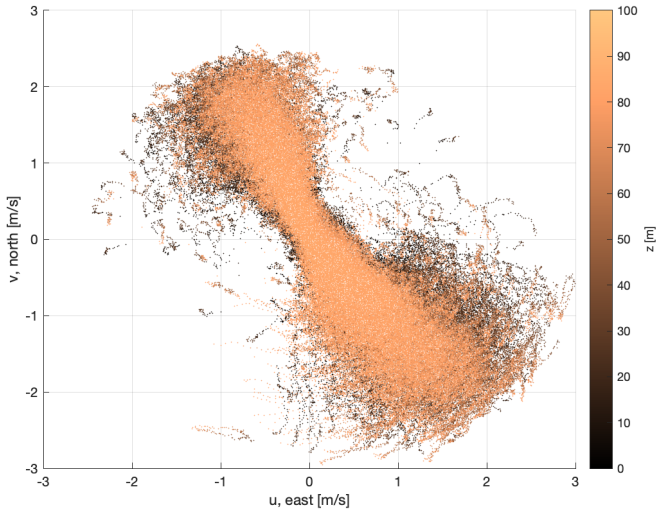

Figure 11: Stablemoor Sig500 horizontal components and principal axes. Color is height of each bin above seafloor z.

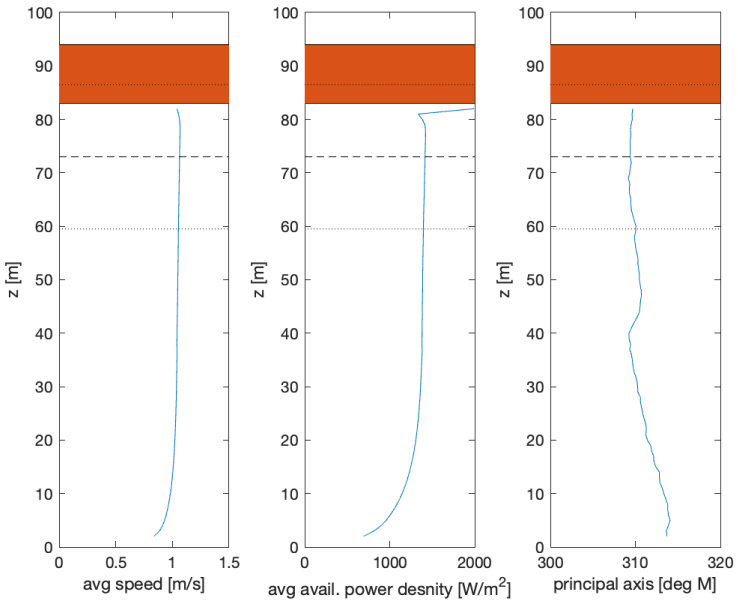

Figure 12: Stablemoor profiles of average speed, available power density, and principal axes. Profile are from merging the up- and down-looking Sig500s.

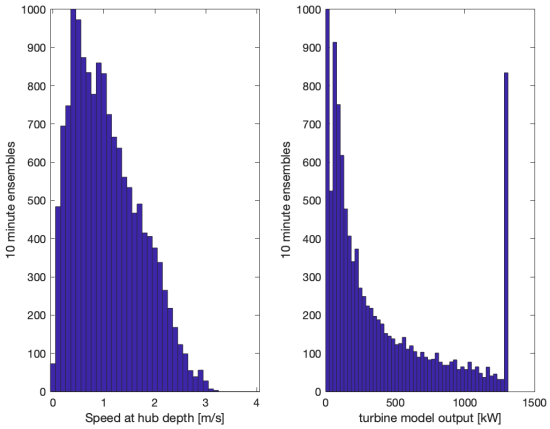

Figure 13: Histograms of hub-depth speed and power production from the Stablemoor.

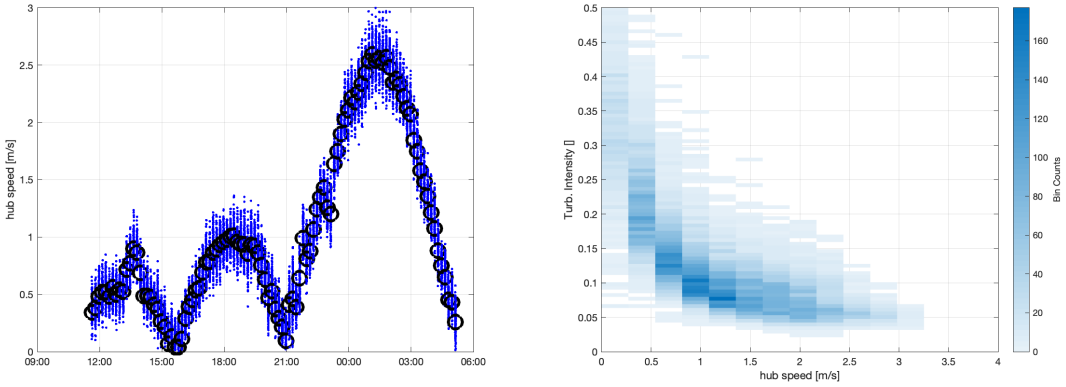

Figure 14: Stablemoor Sig500 example raw time series (left) and turbulent intensity versus speed (right). The blue dots are single-ping data every 1 second, and the black circles are ensembles every 10 minutes.

m below the measured surface (from the depth given by the pressure sensor). A histogram of U_{hub} is shown in Figure 13, along with a histogram of the resulting power from the model turbine (Eq. 3). Both are similar to the Sea Spider results.

The single ping data from the up-looking Sig500 are used to calculate the turbulence statistics of the horizontal speeds at hub depth for each ensemble (Eq. 1). Figure 14 shows an example 2-day time series with single-ping data and ensemble values, along with the TI results from the entire 103-day deployment as a function of hub speed. The Stablemoor TI levels are slightly lower than the Sea Spider results, with values as low as 5% at the higher ensemble speeds. This suggests that either 1) the Doppler noise correction (Eq. 1) used for the Sea Spider results underestimates the apparent variation from Doppler noise, or 2) the motion of Stablemoor filters some of the turbulence.

3.2.3 Surface Buoy

The down-looking Aquadopp mounted to the surface buoy was a measurement-of-opportunity, and the data are lower quality relative to the other platforms. Recall that the primary purpose of the surface buoy was to mark the site and alert tribal fishermen to the presence of the sub-surface Stablemoor nearby. The surface buoy was found with significant amounts of kelp around it during recovery, which may account for some of the reduction in data quality. The kelp was not present during two prior inspection visits in October and November.

The Aquadopp is a much older instrument, with only 3 beams (instead of 5) and narrowband processing (instead of broadband). Thus, there are no extra beams for determine east-north-up velocity components when a beam is obscured, and there are no acoustic correlation values to use in diagnosing bad data. The Aquadopp was mounted with beam 3 always downstream as the mooring aligned with the currents; it appears this beam was contaminated by kelp and possibly bubbles shed by the mooring line (see Appendix). With the third beam questionable, a different approach was used to estimate the horizontal flow speeds using only beams 1 and 2. Beams 1 and 2 faced obliquely upstream and appear to be uncontaminated (see Figure C3). First, the velocity data were transformed to beam coordinates. Assuming the buoy was orientated streamwise, the buoy tilt (mooring angle) was inferred from the apparent vertical component of velocity (i.e., for a level buoy, the vertical velocity should be near zero). Using this angle and the lateral spread of beams 1 and 2, a new estimate of horizontal streamwise speed was obtained. This approach is similar to the two-beam estimate of the horizontal flow made by river ADCPs [Forbush et al., 2016]).

Figure 15 shows the resulting horizontal component of speed. Note that this is shown as a function of depth below the surface d, rather than height above the seabed z. Some of the deeper measurements have been removed during quality control because of low acoustic backscatter. The profiles have more noise than the data from the other platforms, but reveal the same patterns of diurnal inequality and spring-neap cycles. Figure 15 also shows the average profiles, which barely reach to hub depth (dashed line) because of the range limitation in the 1000 kHz ADCP. Despite the reduced data quality, these average profiles show the same uniformity with depth and support the usage of a speed at the hub-depth as representative of the full turbine rotor sweep.

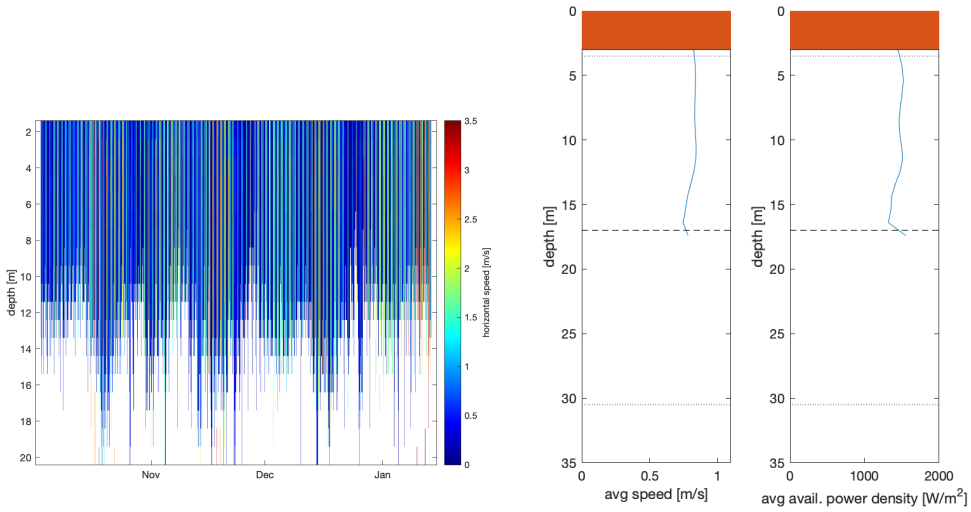

Figure 15: Horizontal speed measured by the Aquadopp on the Surface Buoy (left), and profiles of time-averaged speed and available power density (right).

3.3 Annual Energy Production (AEP) and Capacity Factor (CF) estimates

The stationary observations are used to estimate the AEP and CF following Eqs. 4 and 5. These are presented in Table 2 and compared with results from the FVCOM model of Calandra et al. [2023]. Results are similar using a full annual time series reconstructed using a tidal harmonic analysis of the u, v observations at hub depth. The tidal harmonic analysis is included as an appendix, including exceedance curves and joint probabilities of the velocity components.

Data source	Latitude	Longitude	AEP	Max ensemble speed	CF
Stablemoor	48.56260	-122.76690	5.0 GWh	3.2 m/s	0.22
PNNL FVCOM model	48.5626	-122.7669	5.0 GWh	3.2 m/s	0.22
Sea Spider tripod	48.56270	-122.76510	4.4 GWh	3.2 m/s	0.19
PNNL FVCOM model	48.5628	-122.7650	4.6 GWh	3.1 m/s	0.20
Surface buoy	48.56280	-122.76220	4.0 GWh	3.0 m/s	0.17
PNNL FVCOM model	48.5628	-122.7620	4.0 GWh	2.9 m/s	0.17

Table 2: Annual Energy Production estimates

The reported values are the total for the 'O2' device, which consists of two turbines. Note that FVCOM output was for Apr-May 2017 and that a comparable analysis using the output for June-July 2017 gives similar results. The modeled and measured AEP show excellent agreement and demonstrate the extent of spatial variability in the current resource across the mooring locations.

3.4 Surface Waves

Surface waves were measured by the uplooking Sig500 on the Stablemoor using acoustic surface tracking of the vertical beam [Pederson et al., 2007, Thomson, 2020, Brenner et al., 2023]. Only bulk statistics are shown here, but hourly spectra are included in the NHKDR data submission. There is a data gap from 21-29 Nov 2025, when a raw binary file was corrupted on the instrument for unknown reasons. This affects the wave measurements, not the currents or turbulence.

Figure 16 shows the time series of surface wave heights and peak wave periods. As expected from the limited fetch distances for wave generation and the minimal propagation of swell to the protected site, the waves are relatively small in height and short in period, as compared to open ocean conditions. The largest waves observed were $H_s = 1.8$ m on 14 Dec 2024. This was a historic storm with significant regional impact and can be interpreted as an extreme event.

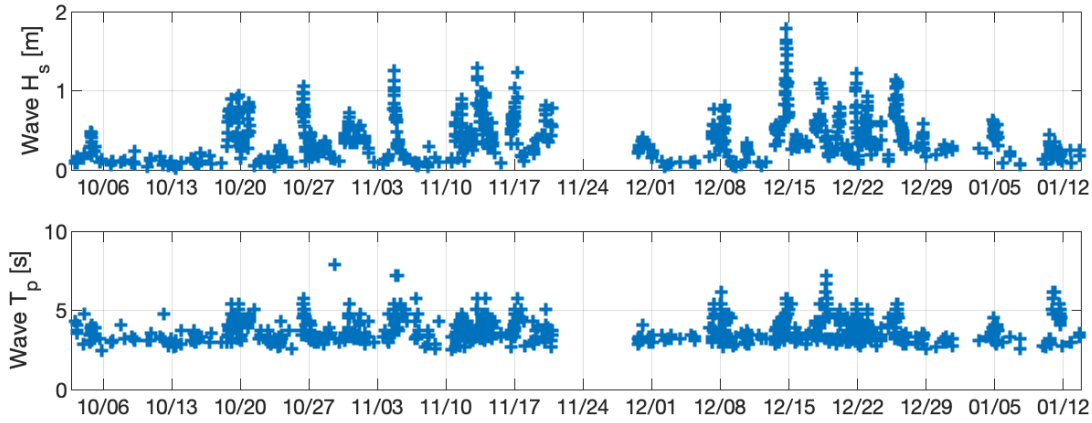

Figure 16: Time series of surface wave heights and peak periods measured from the Stablemoor.

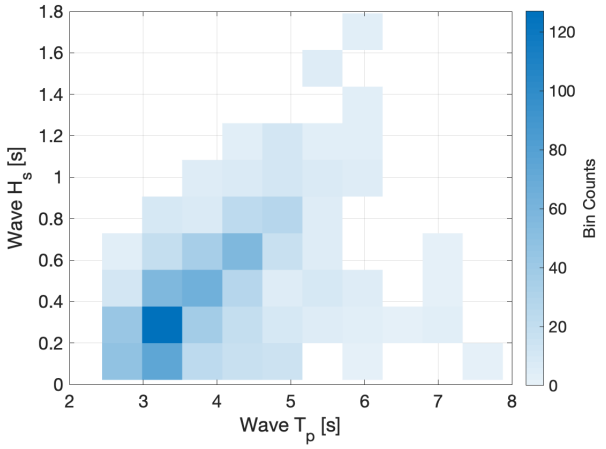

Figure 17: Joint histogram of surface wave heights and peak periods measured from the Stablemoor.

Figure 17 shows a joint histogram of surface wave heights and peak periods. The correlation of H_s, T_p is expected based on both fetch-limited wave evolution [Dobson et al., 1989, Thomson and Rogers, 2014] and the steepness limitation of deep-water waves [Schwendeman et al., 2014, Schwendeman and Thomson, 2015]. The rare observations of small H_s and longer T_p may be small amounts of swell energy refracting to the site, but the effect is minimal.

These wave observations are consistent with prior wave climatology studies in the region [Gemmrich and Pawlowicz, 2020, Yang et al., 2019]. These studies indicate that this resource characterization spans the portion of the annual cycle with the most storm activity (i.e., fall and winter). The other seasons are expected to have less wave activity. Given the short periods and rapid depth attenuation of such waves, the wave climate is unlikely to be a signficant concern for the operation of a tidal turbine at this site. For the extreme condition of $H_s = 1.8$ m, $T_p = 5.8$ s on 14 Dec 2025, the orbital velocities are ≈ 1 m/s at the surface and ≈ 0.12 m/s at hub depth (wavelength is 51 m for $T_p = 5.8$ s).

3.5 Ambient sound levels

Ambient noise measurements were carried out using two Loggerhead Snap recording hydrophones. The units are equipped with High Tech, Inc. (HTI) 96-min hydrophones (serial numbers 4371090 and 4371088) with nominal sensitivities of approximately -170 dB 1V/μPa, including internal preamplifiers. The units were programmed with an additional 11.1 dB gain applied by the analog to digital converter prior to data storage. Underwater noise was recorded for 30 seconds every 10 minutes throughout the deployment at a sampling rate of 44.1 kHz. Comparison between co-temporal measurements showed good agreement and all results presented here are based on results from a single hydrophones.

Several data products were produced for each recording. These included pressure spectral densities and several sound pressure level calculations. All of these products were derived from frequency-domain analysis of each recording. The 30-second .wav files were split into one-second windows with 50% overlap. Each window was demeaned and tapered using a Hann window prior to taking the discrete Fourier transform and calculating the pressure spectral density (PSD). To minimize additional storage requirements, variable band merging was applied following Martin et al. [2021]. Each window was independently processed before averaging the 59 windows to produce the PSD curve.

Pressure spectral density curves were integrated to calculate sound pressure levels according to

$$SPL = 10 \log_{10} \left(\int_{f_1}^{f_2} 10^{\frac{PSD(f)}{10}} df \right) \tag{6}$$

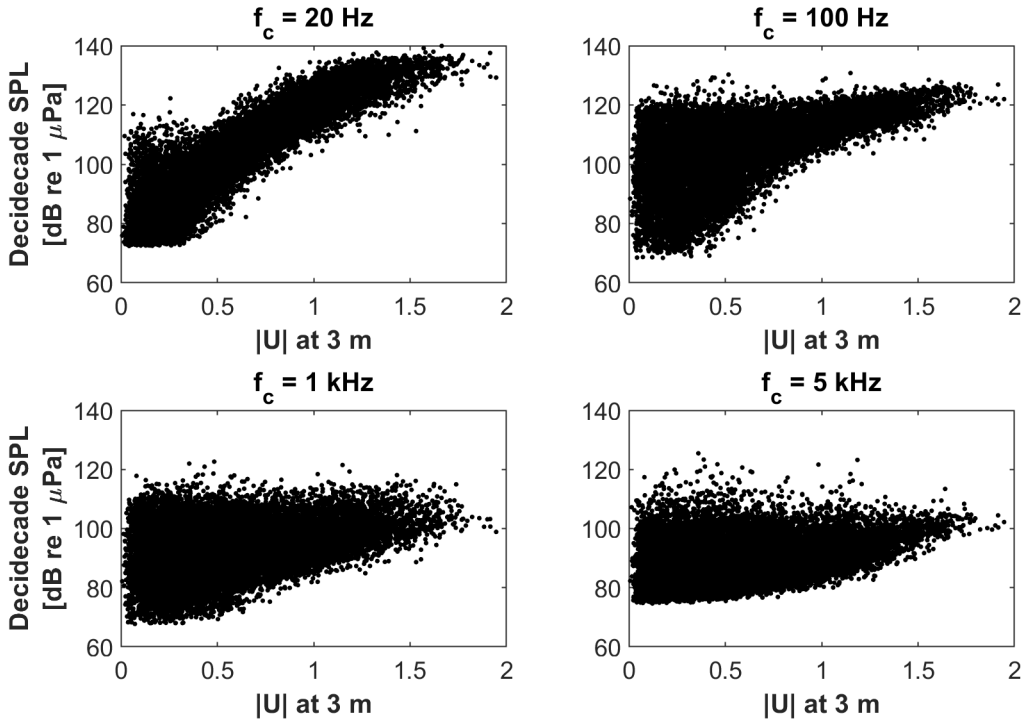

Figure 18: Distributions of decidecade SPLs at four frequencies as a function of frequency. All plots show that for currents below 0.4 m/s the upper and lower limits of measured noise do not change, suggesting flow noise is minimal.

where f_1 and f_2 are arbitrary lower and upper frequency integration limits, SPL has the units of dB re 1μPa and PSD has the units of dB re 1μPa^2/Hz. Broadband sound pressure levels were calculated over two different frequency bands (10-22004 Hz and 500-22004 Hz). The more restricted frequency range was calculated to limit the impacts of flow noise for periods when currents are relatively strong. In additional, decidecade SPLs for center frequency bands 11 Hz to 17.8 kHz were calculated following the standard definitions.

Given that flow noise can contaminate acoustic measurements, particularly at low frequencies [Bassett et al., 2014], additional processing was carried out to identify ambient noise distributions at the site after removing data contaminated by flow noise. By plotting decidecade SPLs against inflow conditions measurement by the ADCP at the closest bin to the hydrophone (3 m above the seabed), a threshold for removal of data of 0.4 m/s was identified. Below this threshold there is no apparent relationship between the lowest noise levels measured and the inflow conditions (Figure 18). The distributions in Figure 18 also indicate that the overall impact of flow noise at frequencies greater than 500 Hz is relatively small.

A time series of broadband sound pressure levels (500 Hz to 20 kHz) is shown in Figure 19. Throughout the deployment, SPLs on the order of 85 dB re 1μPa were recorded regularly while the maximum broadband SPL that was recorded was approximately 134 dB re 1μPa. Noise level did exhibit some dependence on velocity that was not clearly attributed to flow noise as demonstrated by the distributions in Figure 18 and in Figure 19c. This may be attributed to sediment generated noise [Bassett et al., 2013], bubbles entrained due to turbulence, and other unidentified noise sources. To provide a conservative estimate of soundscape variability, further presentations of ambient noise statistics focus on measurements below the 0.4 m/s threshold. This corresponds to 5256 individual recordings or approximately 35.4% of the data.

A shorter timeseries (one day) of current speed and broadband SPLs is shown in Figure 20. While increases in inflow speed do result in a higher noise floor, the highest levels of ambient noise that are

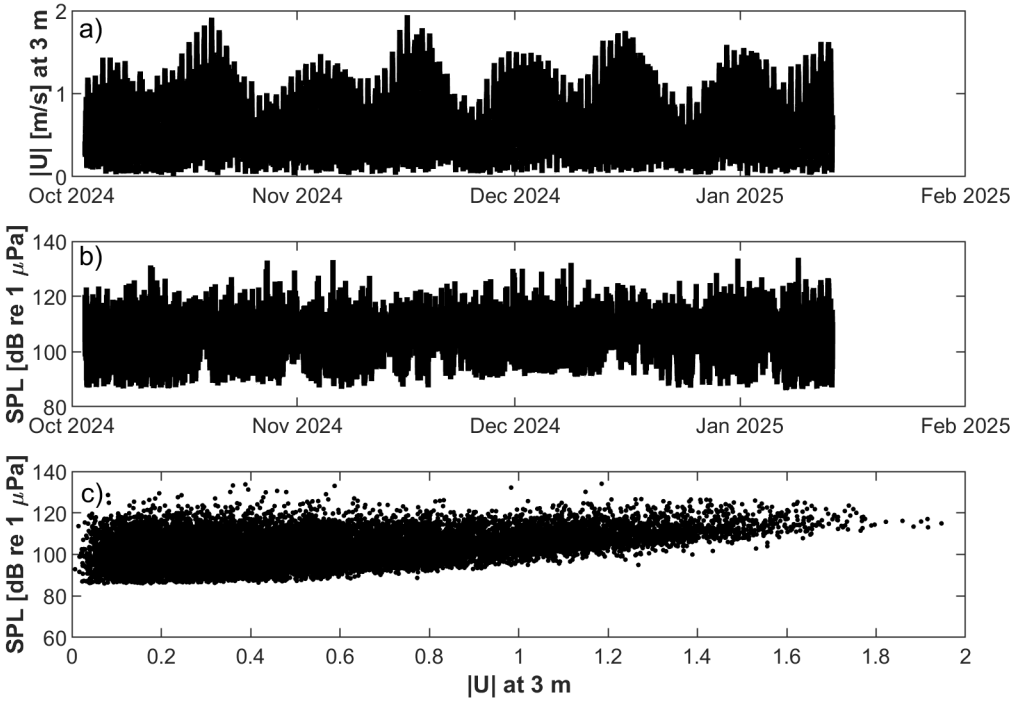

Figure 19: (a) Current speed at 3 m above the seabed. (b) Broadband sound pressure levels (500 Hz to 20 kHz). (c) Broadband sound pressure levels as a function of current speed.

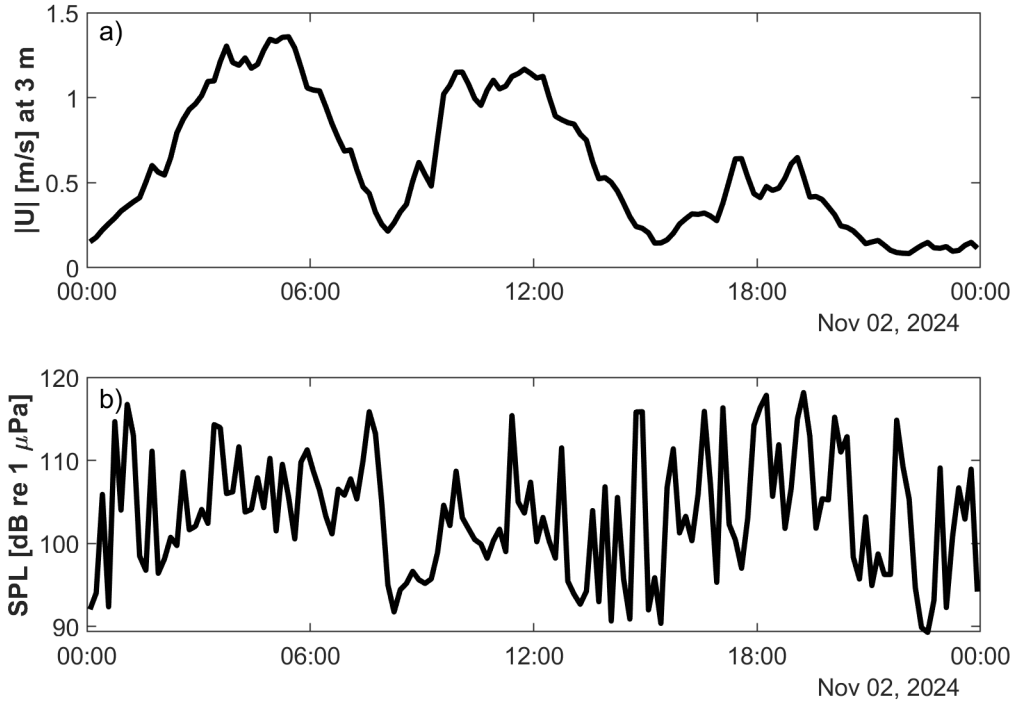

Figure 20: Time series data similar for a single day.

observed are not correlated with the inflow conditions. Noise measurements were made every ten minutes and Figure 20 shows broadband SPLs regularly changed substantially during these periods. While this reveals that the variability in the soundscape was under-resolved at short time scales, we hypothesize that over the multi-month sampling period, the broader statistics likely capture the full distribution of noise at the site.

Broadband (10 Hz to 22 kHz) SPL distributions for measurements below the velocity threshold are shown in Figure 21. The mean broadband SPL calculated for low speeds throughout the deployment was 120.3 dB re 1μPa while the median value was 110.2 dB re 1μPa. The impact of the high intensity levels on the mean is clear in the ECDF, which shows that although the mean broadband SPL is approximately 120 dB re 1μPa, SPLs are lower than the mean approximately 78% of the time (during low flow periods). These are relatively noisy conditions that are consistent with prior observations in the Salish Sea, which attribute elevated SPLs primarily to vessel traffic [Bassett et al., 2012].

Empirical probability density functions for spectral levels at frequencies between 10 Hz and 20 kHz are shown in Figure 22. The highest pressure spectral densities that are regularly observed occur below 100 Hz and are likely attributed to vessel traffic in Rosario Strait. The distribution of observed noise levels generally decreases with frequency with the highest probability pressure spectral densities occurring between approximate 70-90 dB re 1 μPa^2/Hz around 100 Hz, 60-80 dB re 1 μPa^2/Hz around 1000 Hz and between 45-55 dB re 1 μPa^2/Hz around 10 kHz. At frequencies near 10 kHz, frequency-dependent patterns are present in the data. This is likely attributed to self-noise from either the hydrophone or ADCP side bands on the Sea Spider platform. Decidecade noise statistics are presented in Figure 23 and reflect the broader trends identified in the statistics for PSDs.

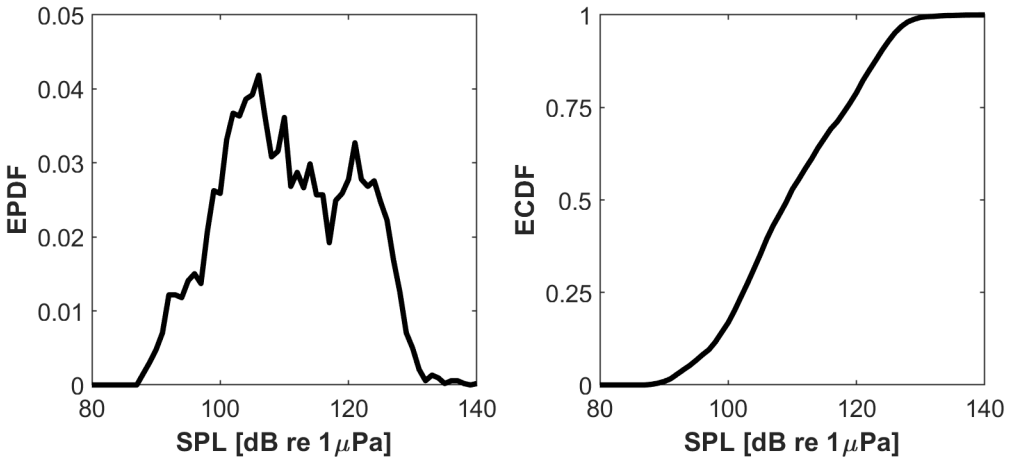

Figure 21: (a) Empirical probability density functions and (b) empirical cumulative distribution functions for broadband noise at low current speeds.

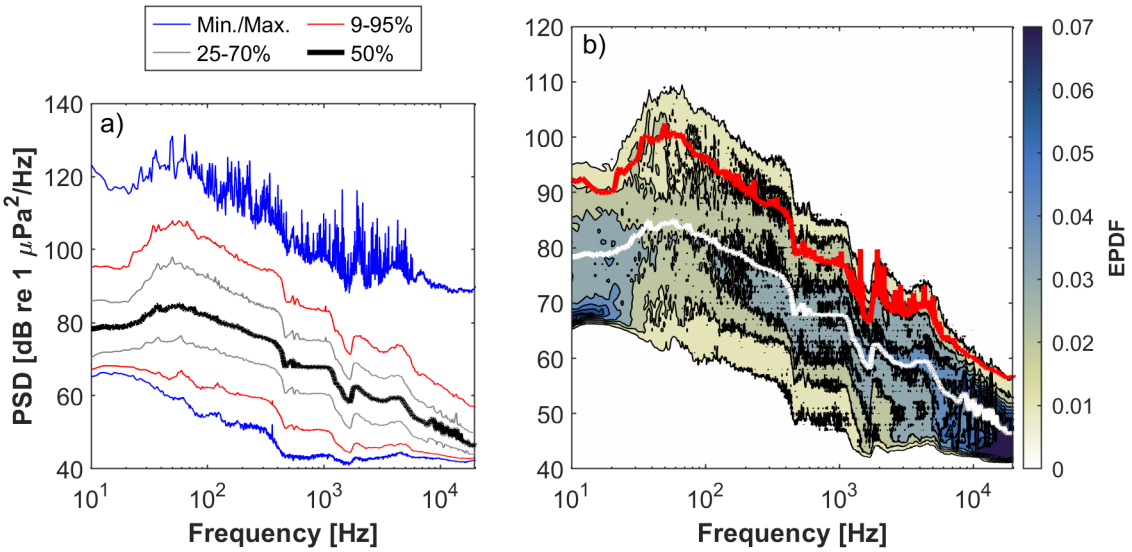

Figure 22: (a) Pressure spectral density statistics. (b) A contour plot of empirical probability density functions of pressure spectral densities. The white and red lines show the median and mean pressure spectral densities, respectively. Both figures are calculated using only data with current speeds below 0.4 m/s.

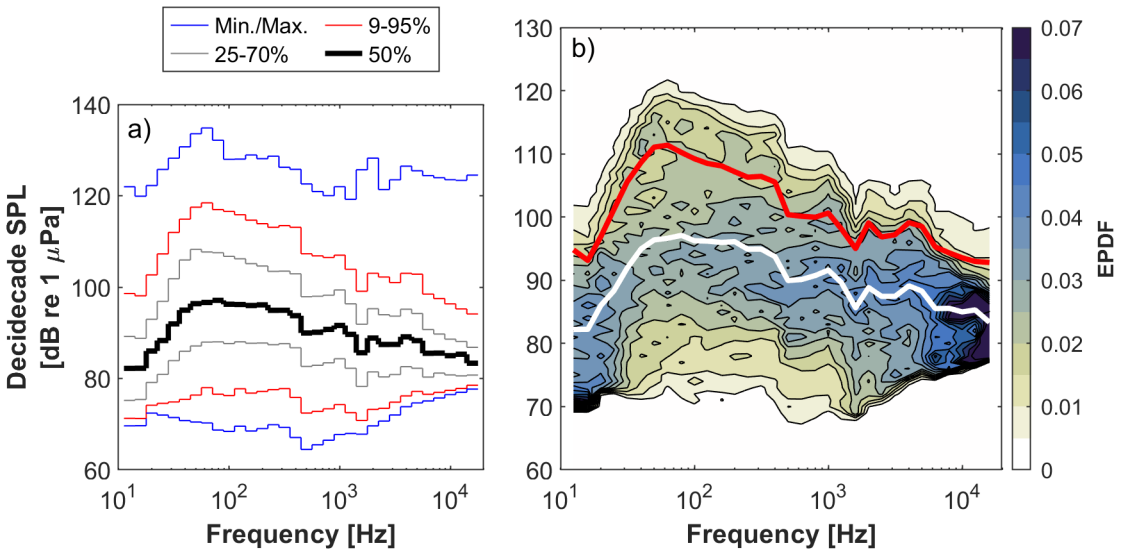

Figure 23: (a) Decidecade SPL statistics. (b) A contour plot of empirical probability density functions of decidecade SPLs. The white and red lines show the median and mean values, respectively. Both figures are calculated for data with current speeds below 0.4 m/s.

3.6 Stratification

The San Juan Islands of Washington State are known to have stratification and estuarine circulations in addition to strong tidal flows [MacCready and Geyer, 2010]. Stratification is monitored at repeat stations throughout the region by the WA State Dept. of Ecology. Typical values are a few PPT salinity change and a few deg C change over 50-200 m depth. The associated estuarine circulations are weak, relative to the tidal currents, and are most prominent during neap tidal cycles [Deppe et al., 2017]. Thus, seasonal variations in stratification at this site are not expected to have a significant effect on the currents or the AEP estimates. Figure 24 shows the data from a CTD (conductivity, temperature, depth) sensor mounted on the Stablemoor (RBR Concerto). These are typical variations for a tidal channel in this region. The clusters, or stripes, in this figure are mixing lines along which water masses are evolving while advecting through the region.

The temperature data from the stationary measurements (Figs. A1 and B1) show tidal variations in the early autumn, then well-mixed conditions (i.e., no variations) in the late fall and early winter. This is expected as autumn storms drive mixing of the full water column, coincident with a lack of solar radiation to provide surface warming.

3.7 Fish tags and porpoise clicks

Opportunistic measurements for tagged fish were included using a Vemco receiver on the Sea Spider tripod. No tagged fish were detected.

Additional opportunistic measurements used 'C-POD' (Chelonia) click detectors with automated onboard processing to listen for marine mammal echolocation and record the details of the click trains associated with each echolocation event. Figure 25 shows detections by species class reported by the manufacturer software. Each click event is assigned an certainty value based on its acoustic characteristics, with subsequent analysis restricted to events with "Hi(gh)" and "Mod(erate)" certainties. Click events are statistically represented through "detection positive minutes" (DPM) (i.e., a minute with at least one click event at a given certainty level). As shown in Figure 25, the only species with routinely high certainty classifications are harbor porpoises. The "low" certainty click events mirror those with "Mod" certainty. "Dolphin" click events, which

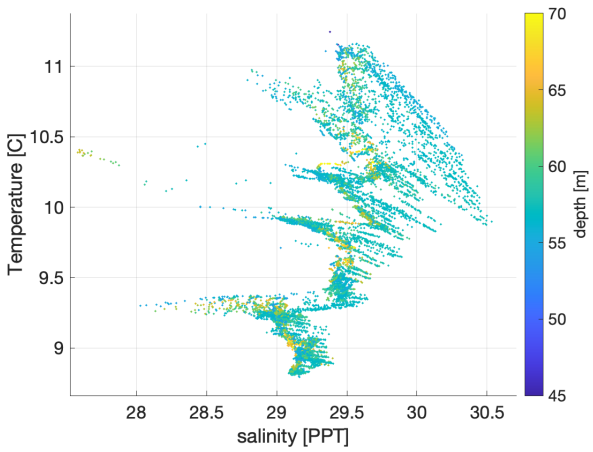

Figure 24: Temperature versus salinity measured on the Stablemoor.

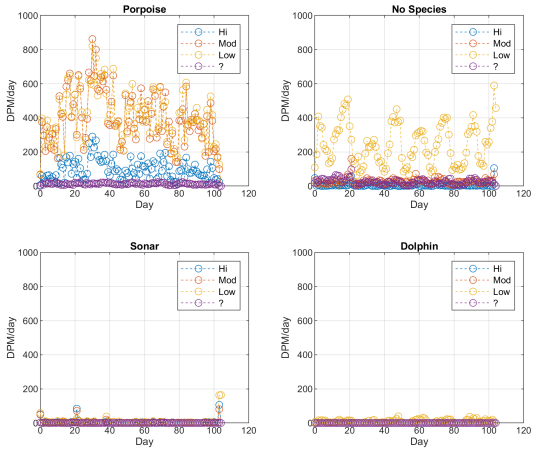

Figure 25: CPOD detections by certainty level and click event type.

would be indicative of killer whale echolocation, are generally absent in the data (only possible classifications are low certainty). Sonars are intermittently detection with moderate to high certainty, potentially associated with subsistence fishing or deployment/retrieval operations by the R/V Robertson. The "No Species" click events are all low certainty and, given the roughly 14-day oscillations may be "clicks" associated with sediment transport during periods with stronger currents [Bassett et al., 2013].

4 Discussion

Other than the region of separated flow close to shore (i.e., the back eddy in Figure 4), the site is well suited for the placement of tidal turbines. The current profiles have minimal shear over the rotor span of the intended O2 turbines, and the turbulent intensity is moderate. The water depths (80-90 m) are feasible for moorings and other in-water work. The wave climate is relatively benign. The principal axes of ebb and flood are almost reciprocal, which is particularly beneficial for the O2 turbine design. The speed histograms are smooth, and the mixed tidal diurnal inequality provides ample work windows for deployment, recovery, and maintenance activity.

The FVCOM model output reported in Calandra et al. [2023] has remarkable accuracy relative to the stationary measurements, with AEP values and maximum speeds in strong agreement. This makes it tempting to target the 'hot spot' shown in the model (Figure 1), which is just northwest of the stationary measurement sites. However, the mobile survey indicates that this is also where the flow begins to separate and shed eddies at the corner of the island. Further, the acceleration of flow is sufficiently localized that the momentum extraction from the turbines might alter the flow sufficiently to displace the hot spot. For these reasons, it seems more prudent to target the quasi-homogeneous region surveyed by the stationary measurements, where the flow is rectilinear and the bathymetry is smooth.

5 Conclusion

The OPALCO site at the western edge of Rosario Strait (WA, USA) has been characterized for potential tidal current power generation. Stationary and mobile measurements using ADCPs have determined the flow conditions and Annual Energy Production (AEP). The Sea Spider results satisfied the IEC 62600-201 standard. Additional measurements from Stablemoor and surface buoy moorings expanded the spatial context and improved the turbulence characterization. A prior numerical modeling study has strong agreement with the measurements.

Overall, the site is well-suited to tidal current power generation. A minimum AEP of 4.0 GWh can be expected from two turbines, and up to 5.0 GWh is feasible.

6 Data and software archive

All data, processing code, and results have been submitted to MHKDR (Marine Hydrokinetic Data Repositor) as submission #609.
`https://mhkdr.openei.org/submissions/609`.

Some analysis codes from public GitHub libraries also were used, including
`https://github.com/SASlabgroup/SWIFT-codes/Waves/UVZwaves.m` and
`https://github.com/SASlabgroup/NortekCodes/blob/main/Signature/sigProcess_all.m`.

7 Acknowledgments

Joe Talbert, Alex de Klerk, and Amy Larson completed the design, rigging, and fabrication of the deployment platforms. Andy Ellers and Anna McBee operated the R/V Jack Robertson. Malcolm LeClair, Christie Hegermiller, Ari Athair, Sarah Palmer, Jayden Wood, Fiona Drum, and Aidan Hunt assisted with the deployments and recoveries. 48 North Solutions provided permitting support.

References

Gemma Calandra, Taiping Wang, Calum Miller, Zhaoqing Yang, and Brian Polagye. A comparison of the power potential for surface- and seabed-deployed tidal turbines in the san juan archipelago, salish sea, wa. *Renewable Energy*, 214:168–184, 2023. ISSN 0960-1481. doi: https://doi.org/10.1016/j.renene.2023.05.099. URL https://www.sciencedirect.com/science/article/pii/S0960148123007322.

J. McVey, L. Kilcher, J. Thomson, and Z. Yang. Turbulence measurements at three potential tidal energy sites in the salish sea. *Applied Ocean Research*, in minor revision, 2025.

B. H. Brumley, R. G. Cabrera, K. L. Deines, and E. A. Terray. Performance of a broad-band acoustics Doppler current profiler. *J. Ocean. Eng.*, 16(4), 1991.

M. Palodichuk, B. Polagye, and J. Thomson. Resource mapping at tidal energy sites. *J. Ocean. Eng.*, 38 (3):433–446, July 2013. doi: 10.1109/JOE.2012.2227578.

R. Pawlowicz, R. Beardsley, and S. Lentz. Classical tidal harmonic analysis include error estimates in MATLAB using T-TIDE. *Computers and Geosciences*, 28(8):929–937, 2002.

B. Polagye and J. Thomson. Tidal energy resource characterization: methodolgy and field study in Admiralty Inlet, Puget Sound, USA. *Proc. IMechE, Part A: J. Power and Energy*, 227(3):352–367, 2013. doi: 10.1177/0957650912470081.

J. Thomson, B. Polagye, V. Durgesh, and M. Richmond. Measurements of turbulence at two tidal energy sites in Puget Sound, WA. *J. Ocean. Eng.*, 37(3):363–374, 2012. URL https://doi.org/10.1109/JOE.2012.2191656.

Maricarmen Guerra and Jim Thomson. Turbulence measurements from five-beam acoustic doppler current profilers. *Journal of Atmospheric and Oceanic Technology*, 34(6):1267–1284, 2017. doi: 10.1175/JTECH-D-16-0148.1. URL https://doi.org/10.1175/JTECH-D-16-0148.1.

Samuel Harding, Levi Kilcher, and Jim Thomson. Turbulence measurements from compliant moorings. part i: Motion characterization. *Journal of Atmospheric and Oceanic Technology*, 34(6):1235–1247, 2017. doi: 10.1175/JTECH-D-16-0189.1. URL https://doi.org/10.1175/JTECH-D-16-0189.1.

Levi F. Kilcher, Jim Thomson, Samuel Harding, and Sven Nylund. Turbulence measurements from compliant moorings. part ii: Motion correction. *Journal of Atmospheric and Oceanic Technology*, 34(6):1249–1266, 2017. doi: 10.1175/JTECH-D-16-0213.1. URL https://doi.org/10.1175/JTECH-D-16-0213.1.

Samuel Brenner, Luc Rainville, Jim Thomson, Sylvia Cole, and Craig Lee. Comparing observations and parameterizations of ice-ocean drag through an annual cycle across the beaufort sea. *Journal of Geophysical Research: Oceans*, n/a(n/a):e2020JC016977, 2021. doi: https://doi.org/10.1029/2020JC016977. URL https://agupubs.onlinelibrary.wiley.com/doi/abs/10.1029/2020JC016977. e2020JC016977 2020JC016977.

SJ Lentz, A Kirincich, and AJ Plueddemann. A note on the depth of sidelobe contamination in acoustic doppler current profiles. *Journal of Atmospheric and Oceanic Technology*, 39(1):31–35, 2022.

P.J. Wiles, T. P. Rippeth, J.H. Simpson, and P.J. Hendricks. A novel technique for measuring the rate of turbulent dissipation in the marine environment. *Geophys. Res. Let.*, 33:L21608, 2006.

Christopher Bassett, Jim Thomson, and Brian Polagye. Sediment–generated noise and bed stress in a tidal channel. *Journal of Geophysical Research: Oceans*, pages n/a–n/a, 2013. ISSN 2169-9291. doi: 10.1002/jgrc.20169. URL http://dx.doi.org/10.1002/jgrc.20169.

Dominic Forbush, Brian Polagye, Jim Thomson, Levi Kilcher, James Donegan, and Jarlath McEntee. Performance characterization of a cross-flow hydrokinetic turbine in sheared inflow. *International Journal of Marine Energy*, 16:150 – 161, 2016. ISSN 2214-1669. doi: http://dx.doi.org/10.1016/j.ijome.2016.06.001. URL http://www.sciencedirect.com/science/article/pii/S2214166916300455.

T. Pederson, E. Siegel, and J. Wood. Directional wave measurements from a subsurface buoy with an acoustic wave and current profiler (awac). In *Proceedings Oceans 2007, Vancouver, Canada.*, 2007.

Jim Thomson. Long-term measurements of ocean waves and sea ice draft in the central beaufort sea. Technical Report TM 1-20, Applied Physics Laboratory, University of Washington, 2020.

Samuel Brenner, Jim Thomson, Luc Rainville, Daniel Torres, Martin Doble, Jeremy Wilkinson, and Craig Lee. Acoustic sensing of ocean mixed layer depth and temperature from uplooking adcps. *Journal of Atmospheric and Oceanic Technology*, 40(1):53 – 64, 2023. doi: 10.1175/JTECH-D-22-0055.1. URL https://journals.ametsoc.org/view/journals/atot/40/1/JTECH-D-22-0055.1.xml.

F. Dobson, W. Perrie, and B. Toulany. On the deep-water fetch laws for wind-generated surface gravity waves. *Atmos.-Ocean*, 27:210–236, 1989.

Jim Thomson and W. Erick Rogers. Swell and sea in the emerging Arctic Ocean. *Geophysical Research Letters*, 41(9), 2014. ISSN 1944-8007. doi: 10.1002/2014GL059983. URL http://dx.doi.org/10.1002/2014GL059983.

M. Schwendeman, J. Thomson, and J. Gemmrich. Wave breaking dissipation in a young wind sea. *J. Phys. Oceanogr.*, 44(1):104–127, 2014.

Michael Schwendeman and Jim Thomson. Observations of whitecap coverage and the relation to wind stress, wave slope, and turbulent dissipation. *Journal of Geophysical Research: Oceans*, pages n/a–n/a, 2015. ISSN 2169-9291. doi: 10.1002/2015JC011196. URL http://dx.doi.org/10.1002/2015JC011196.

J. Gemmrich and R. Pawlowicz. Wind waves in the strait of georgia. *Atmosphere-Ocean*, 0(0):1–19, 2020. doi: 10.1080/07055900.2020.1735989. URL https://doi.org/10.1080/07055900.2020.1735989.

Zhaoqing Yang, Gabriel García-Medina, Wei-Cheng Wu, Taiping Wang, L. Ruby Leung, Luca Castrucci, and Guillaume Mauger. Modeling analysis of the swell and wind-sea climate in the salish sea. *Estuarine, Coastal and Shelf Science*, 224:289 – 300, 2019. ISSN 0272-7714. doi: https://doi.org/10.1016/j.ecss.2019.04.043. URL http://www.sciencedirect.com/science/article/pii/S0272771419301556.

S. Bruce Martin, Briand J. Gaudet, Holger Klinck, Peter J. Dugan, Jennifer L. Miksis-Olds, David K. Mellinger, David A. Mann, Olaf Boebel, Colleen C. Wilson, Dimitri W. Ponirakis, and Hilary Moors-Murphy. Hybrid millidecade spectra: A practical format for exchange of long-term ambient sound data. *JASA Express Letters*, 1(1):011203, 01 2021. ISSN 2691-1191. doi: 10.1121/10.0003324. URL https://doi.org/10.1121/10.0003324.

C. Bassett, J. Thomson, P. Dahl, and B. Polagye. Flow-noise and turbulence in two tidal channels. *J. Acoust. Soc. Am.*, 135(4):1764–1774, 2014. doi: http://dx.doi.org/10.1121/1.4867360.

C. Bassett, B. Polagye, M. Holt, and J. Thomson. A vessel noise budget for admiralty inlet, puget sound, washington (usa). *J. Acoust. Soc. Am.*, 132(6), 2012. URL https://doi.org/10.1121/1.4763548.

P. MacCready and W. R. Geyer. Advances in estuarine physics. *Annual Review of Marine Science*, 2:35–38, 2010. URL 10.1146/annurev-marine-120308-081015.

R. Walter Deppe, Jim Thomson, Brian Polagye, and Christopher Krembs. Predicting deep water intrusions to puget sound, wa (usa), and the seasonal modulation of dissolved oxygen. *Estuaries and Coasts*, pages 1–14, 2017. ISSN 1559-2731. doi: 10.1007/s12237-017-0274-6. URL http://dx.doi.org/10.1007/s12237-017-0274-6.

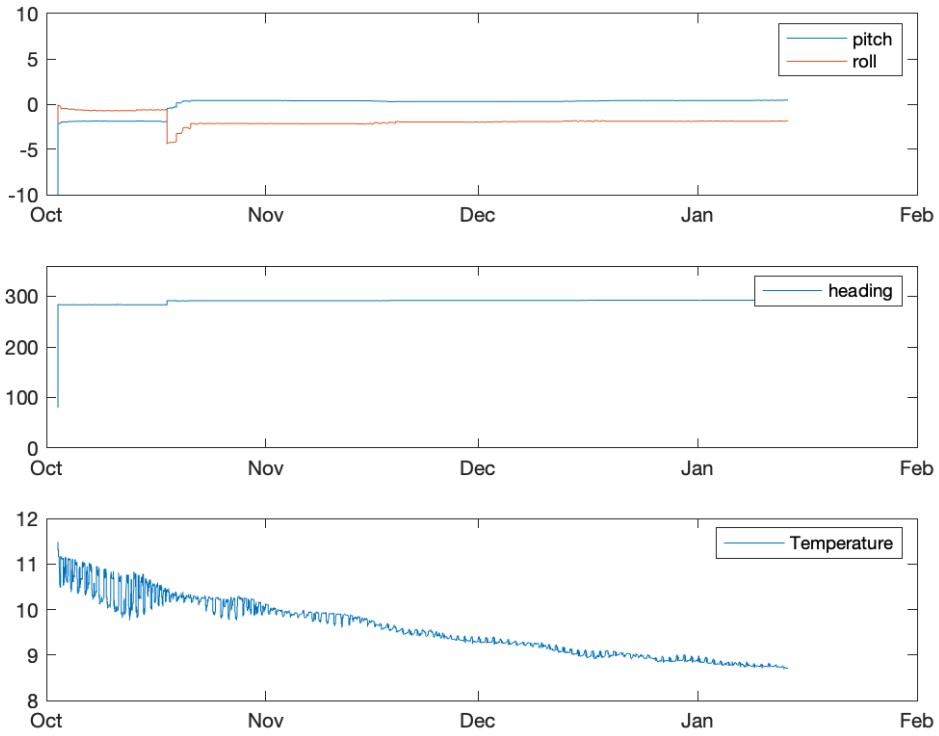

Figure A1: Sea Spider tripod Sig250 ancillary data.

A Quality control / assurance of Sea Spider tripod data

The ancillary data from the Sig250 in Figure A1 suggest no significant motion or turning of the Sea Spider tripod, other than a few degrees of settling during the first spring tide of the deployment. The water temperatures show expected tidal advection in the fall and then fully mixed conditions in the winter.

The backscatter amplitude data from the Sig250 in Figure A2 show an expected decrease with range and strong surface reflections around the black line showing the depth indicated by the pressure gauge. The red line shows the cutoff range $z = d\cos(\theta)$ used to avoid surface reflections. There are no anomalies in the backscatter and no indications of occlusion.

The broadband correlation data from the Sig250 in Figure A3 show nearly 100% correlation for all beams at all depths and at all times. Again, the surface screening shown by the red line appears to catch all surface contaminated bins.

The velocity components shown in Figure A4 show clear tidal signals without discontinuities. The surface bins have been removed above the red line in the previous figures. There is a [probably] spurious signal in the vertical velocity component around $z = 30$ m in the last month of deployment. The consistent depth of the spurious signal suggests that it is self-generated, such as a secondary reflection from the surface or other interference. This spurious signal is small (0.2 m/s) and does not appear to affect horizontal current measurement. Further, it is below the rotor sweep of the intended turbine.

The vertical velocity discrepancy from the Sig250 is shown in Figure A5. This is the difference between the two distinct estimates of vertical velocity that arise from the coordinate transform of the four slanted beams. The values are expected to be small, unless there are significant velocity gradients (i.e., inhomogeneity)

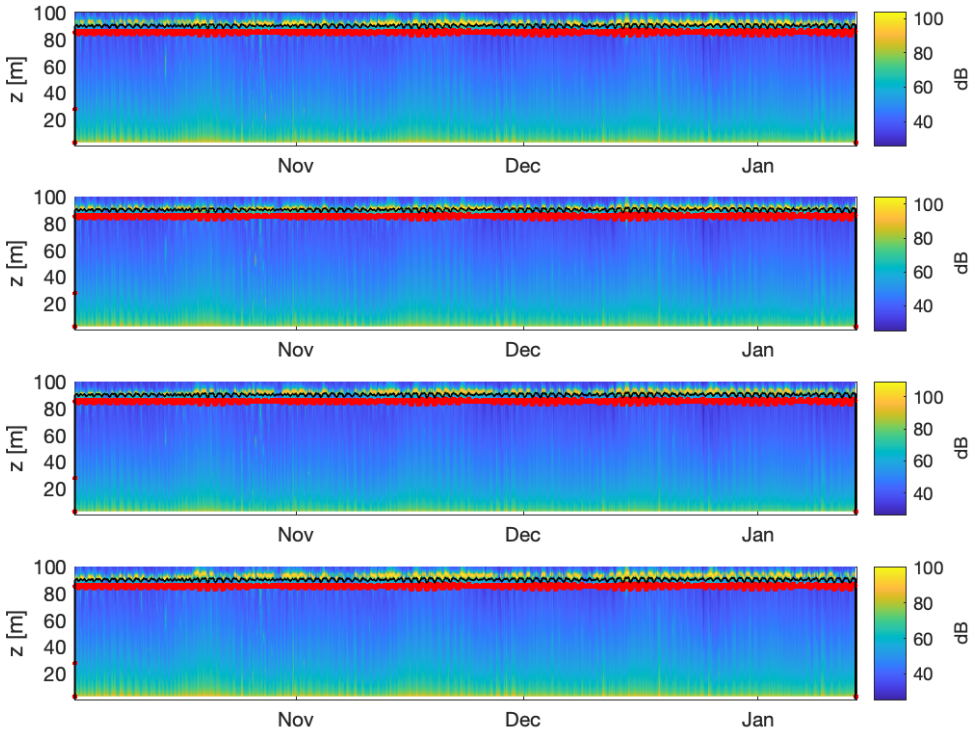

Figure A2: Sea Spider tripod Sig250 backscatter amplitude.

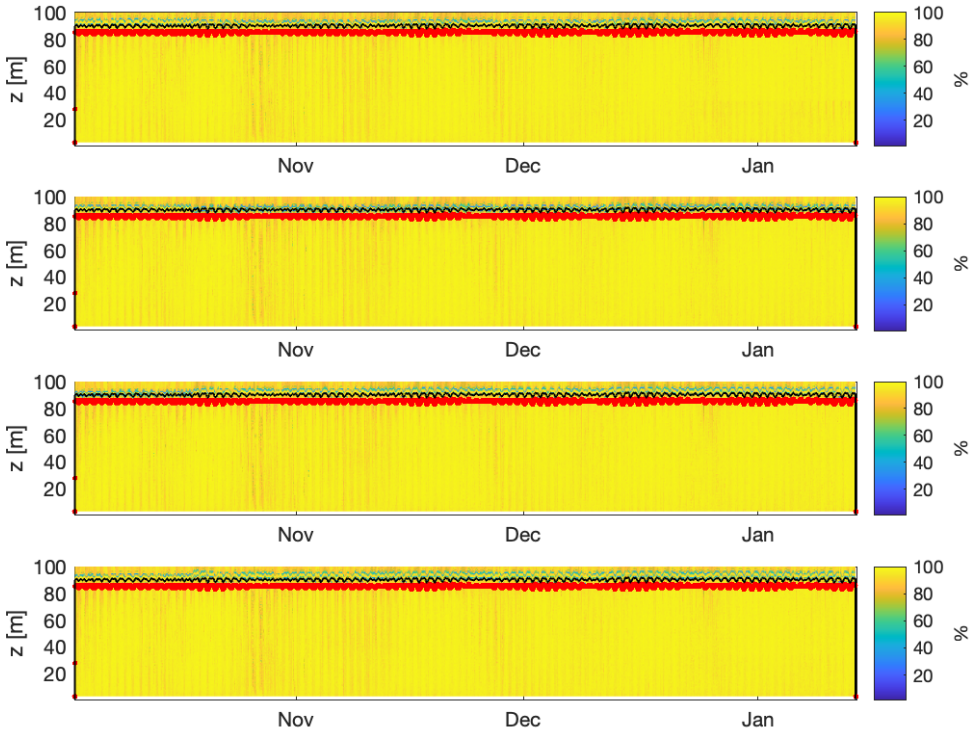

Figure A3: Sea Spider tripod Sig250 Doppler correlations.

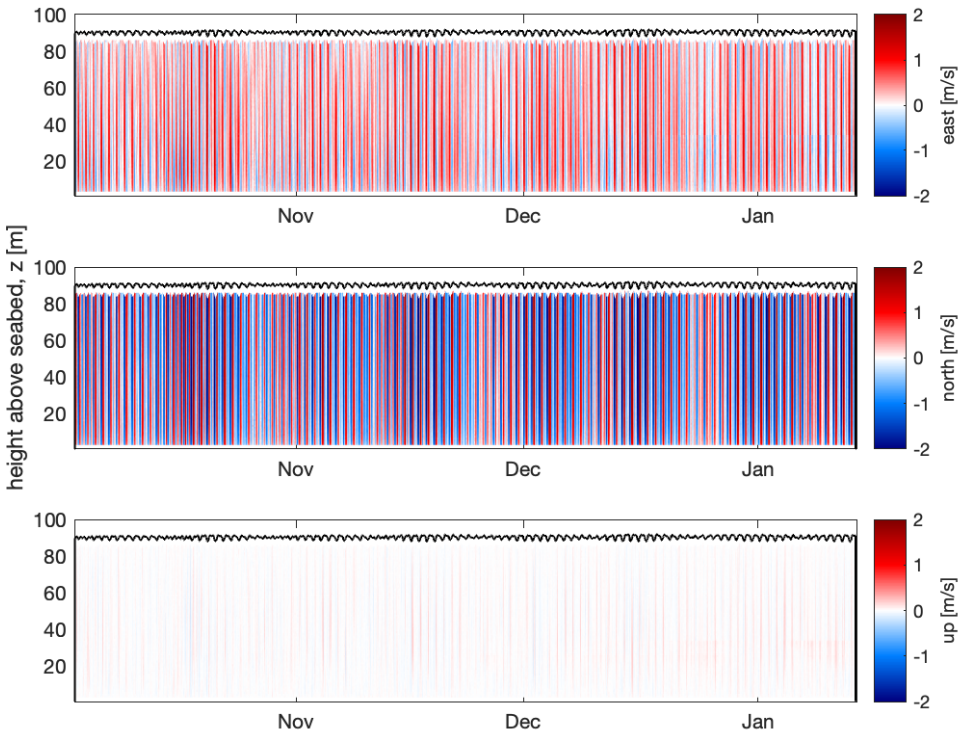

Figure A4: Sea Spider tripod Sig250 profiles of velocity components.

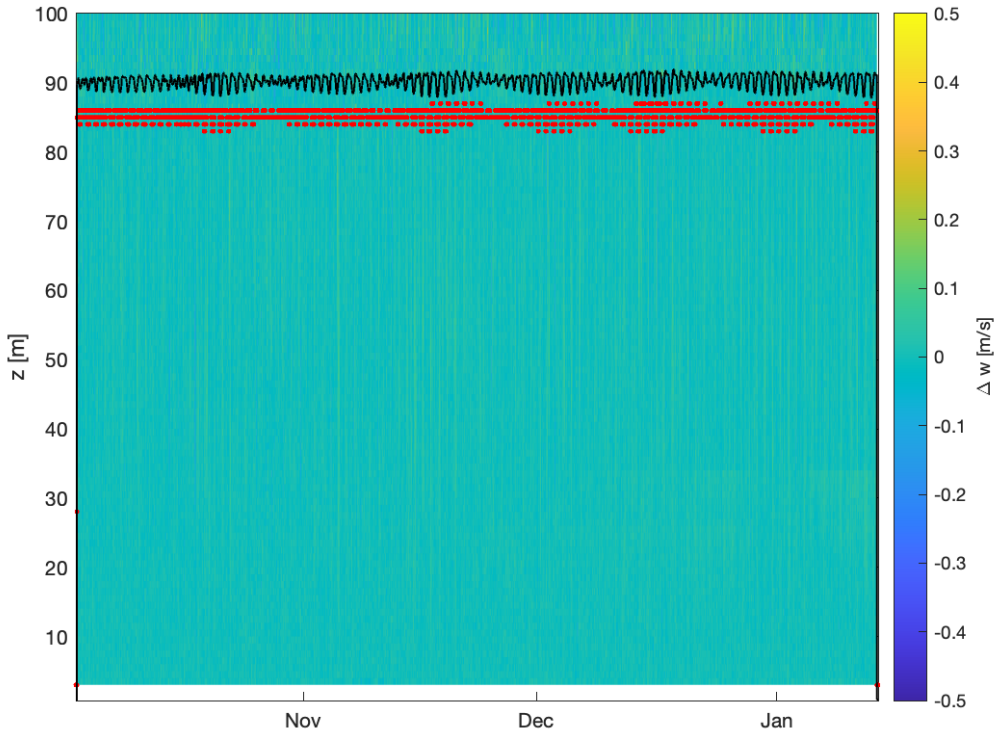

Figure A5: Sea Spider tripod Sig250 vertical velocity error estimates.

within the cone of the ADCP beams or there is bad data from a particular beam. The values here are mostly within the intended precision ±0.05 m / s for all velocity components. The spurious signal at $z \approx 30$ m in Jan 2025 is subtle, but present.

B Quality control / assurance of Stablemoor data

Here follow figures for the Stablemoor that are similar to the preceding Sea Spider quality control figures, with the notable difference that all Stablemoor data are presented as a merged product of the two Sig500s (up- and down-looking). A black line indicates the Stablemoor height above the seafloor through these figures. There is, of course, more motion in Figure B1 because the Stablemoor adjusts to the currents. The backscatter amplitudes decay symmetrically away from the Stablemoor in Figure B2 and the Doppler correlations are universally high in Figure B3. The velocity components in Figure B4 show the enhanced vertical velocities, relative to the Sea Spider measurements, which are related to platform motion. However, testing a three-dimensional scalar speed ($\sqrt{u^2 + v^2 + w^2}$) has negligible effect on the AEP and CF calculations, relative to a two-dimensional scalar speed, so the differences between these values for the Stabloor and Sea Spider are likely spatial variability, not a measurement or processing artifact. The vertical velocity discrepancies in Figure B5 are universally small.

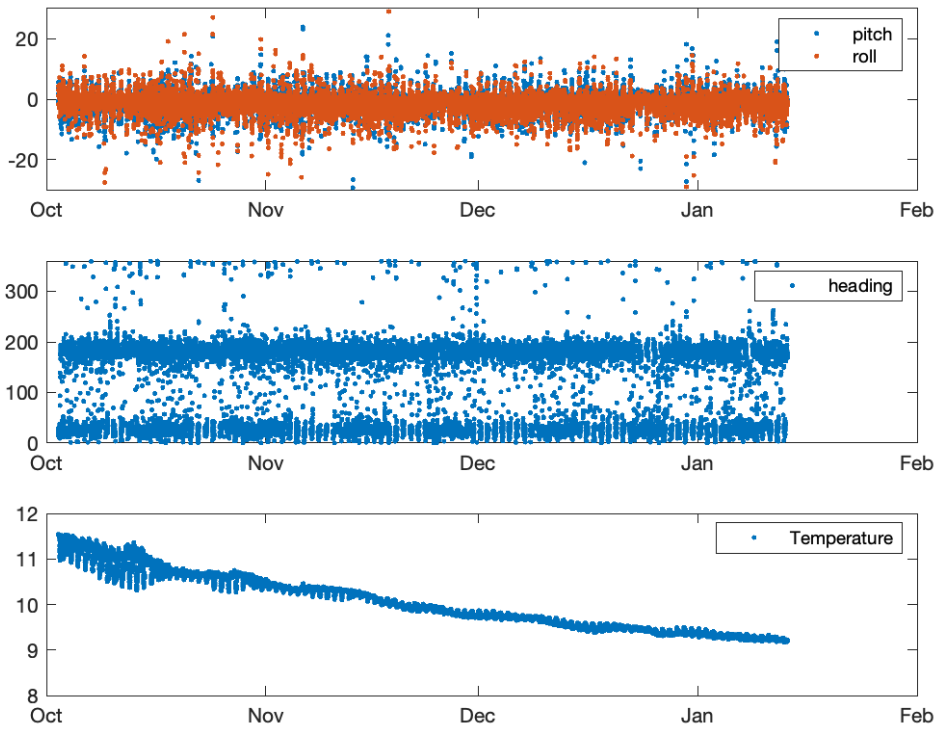

Figure B1: Stablemoor pitch and roll, heading, and water temperature.

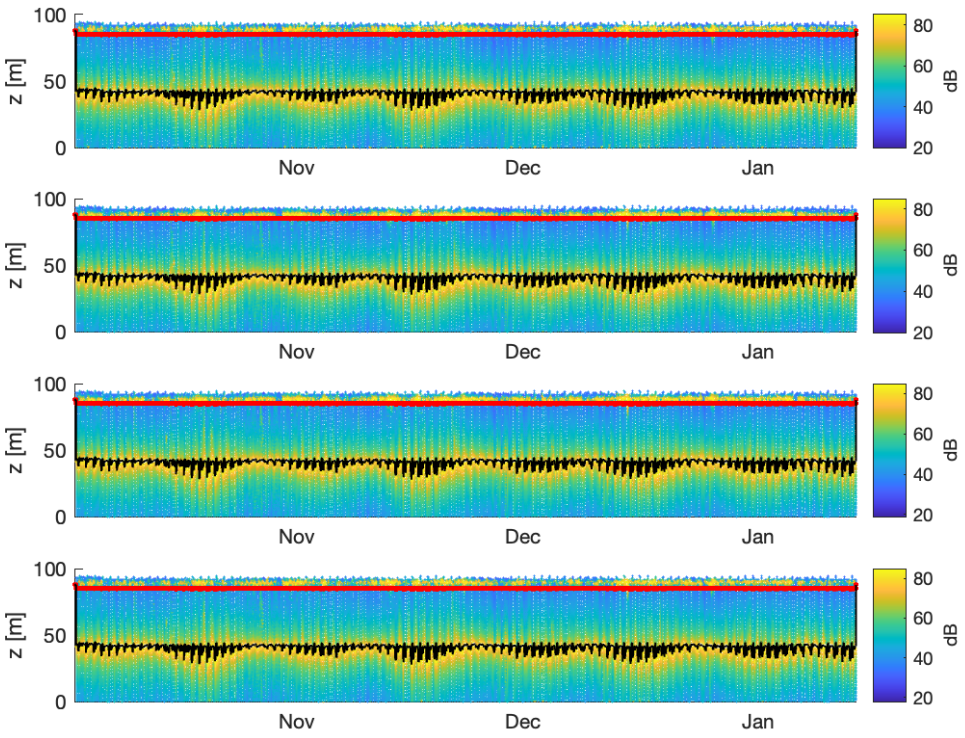

Figure B2: Stablemoor merged Sig500s backscatter amplitude.

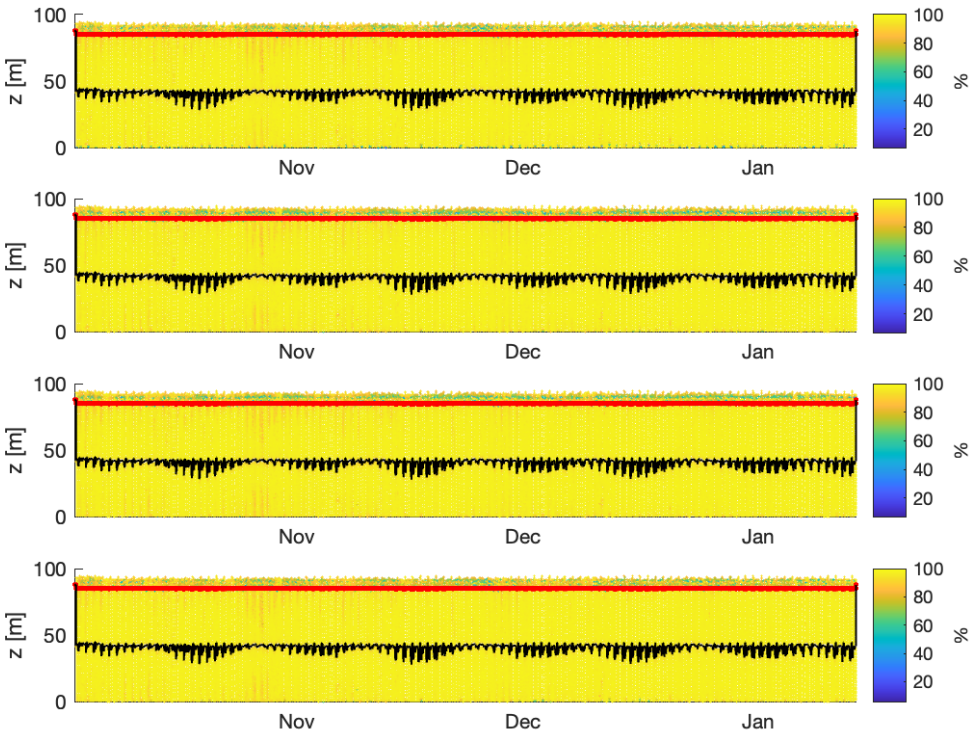

Figure B3: Stablemoor merged Sig500s Doppler correlation.

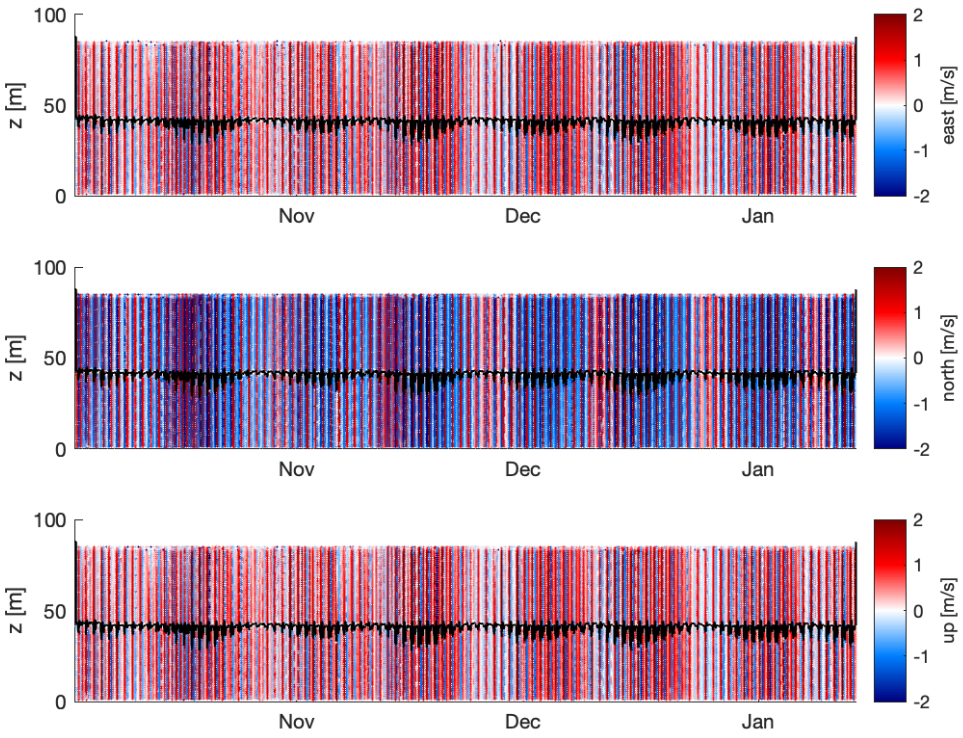

Figure B4: Stablemoor merged Sig500s velocity components.

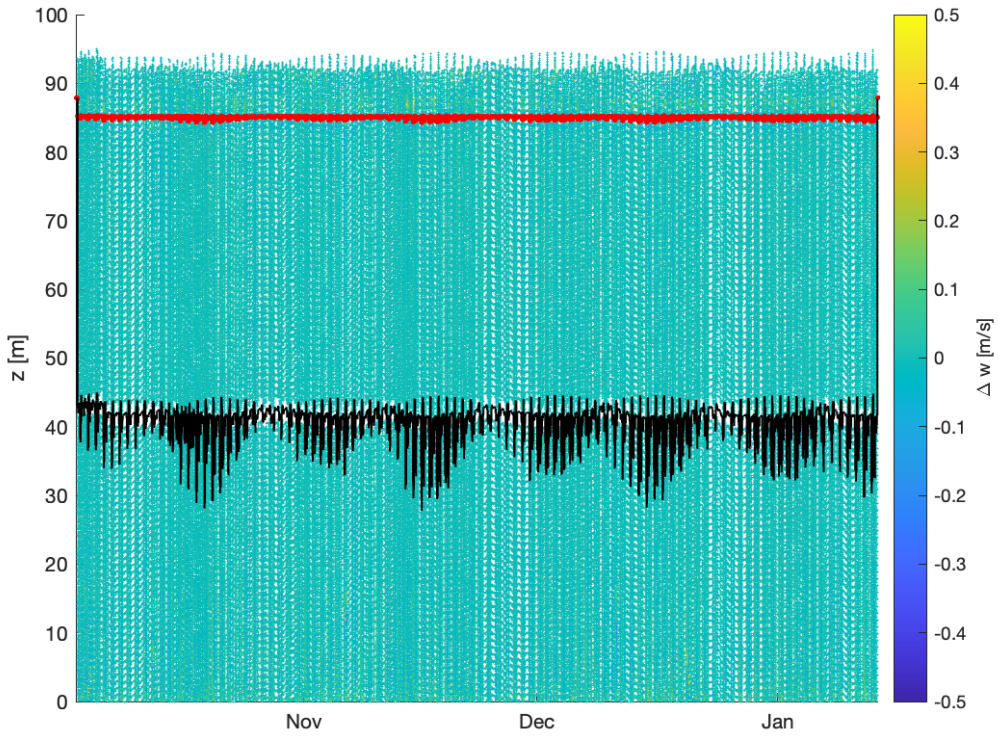

Figure B5: Stablemoor merged Sig500s vertical velocity error estimates.

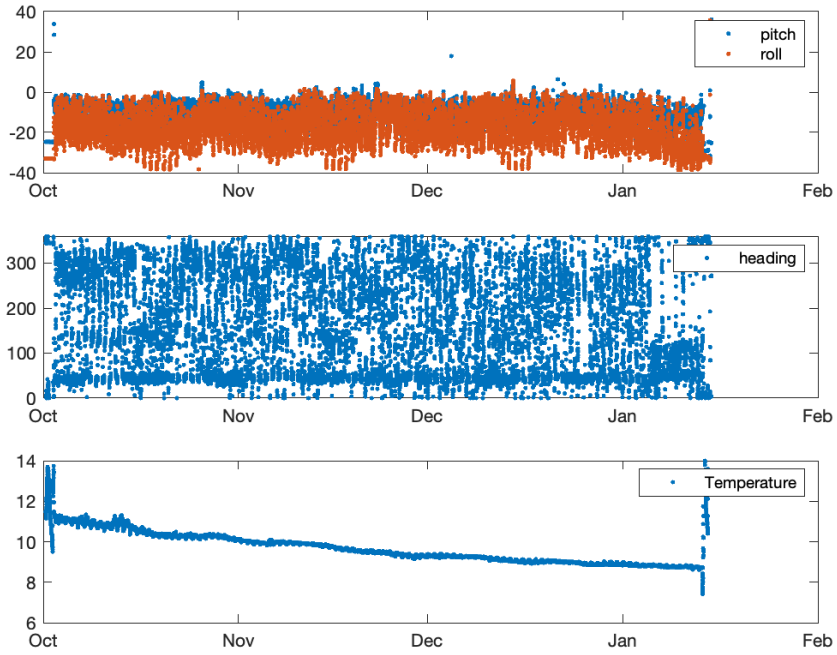

Figure C1: Surface buoy Aquadopp pith and roll, heading, and temperature.

C Quality control / assurance of Surface Buoy data

The Surface Buoy Aquadopp motion in Figure C1 has larger variations than the Stablemoor because the spherical buoy is not streamlined and sheds vorticies. The Aqaudopp backscatter amplitude in Figure C2 has a notable reduction in beam 3, which is the downstream beam (and thus most likely to be obscured). Converting to beam coordinates for Figure C3 shows spurious velocities in beam 3, which prompted the two-beam solution described in the Results.

There is no correlation plot for the Aquadopp, because it is narrow-band Doppler system. There is not vertical erorr Δw plot because Aquadopp is only a 3-beam system (and multiple w estimates requires 4 or 5 beams).

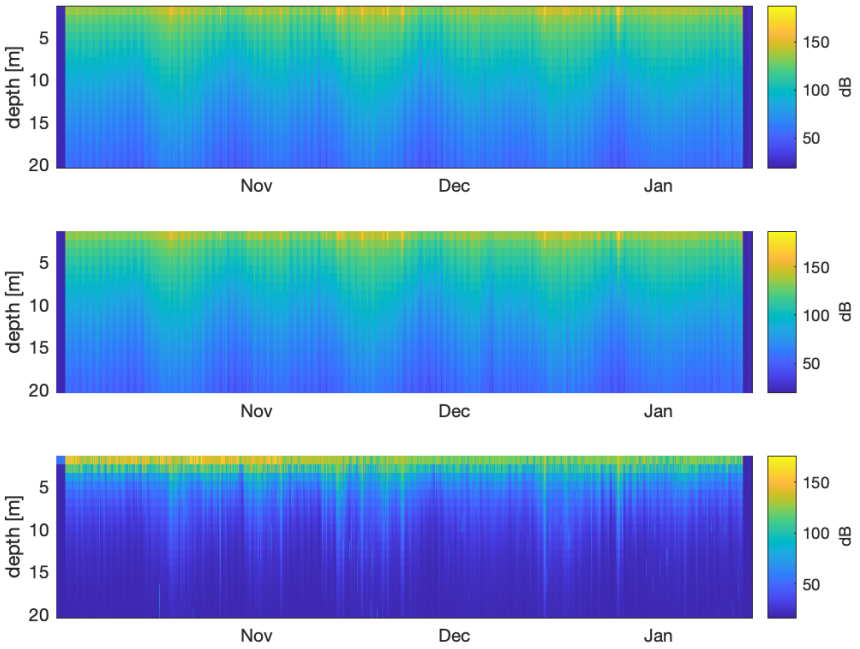

Figure C2: Surface buoy Aquadopp amplitude.

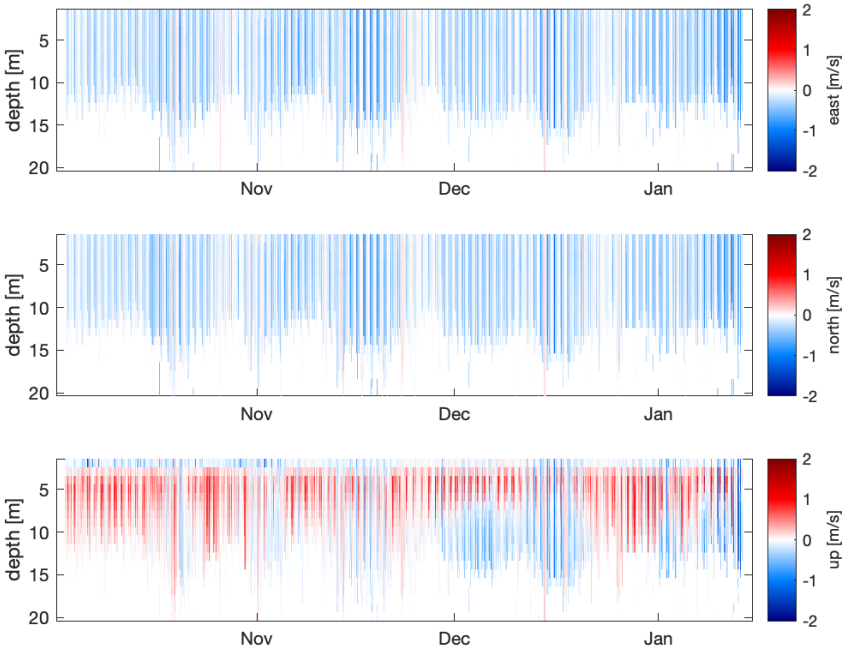

Figure C3: Surface buoy Aquadopp velocity components, in beam coordinates.

D Tidal Harmonic Analysis

Tidal harmonic analysis using T-Tide v1.5b [Pawlowicz et al., 2002] resolved 35 constituents, including the M10 optional constituent for nonlinear flow in shallow channels. The inputs were the u, v components at hub depth as measured by the Sig250 on the Sea Spider. (Tn T-tide, these are input as a complex-valued vector $u + vi$.) The reconstructed velocities capture 96% variance of the original data, when compared over the same 103 day record.

Figure D1 shows the joint probabilities of velocity components from the reconstruction and from the data. The principal axes and distributions are similar, though there is more off-axis variation in the observations. This is likely related to larger scale turbulent eddies, which can cause biases in the two-minute ensembles of the observations relative to the hourly values from the harmonic reconstruction.

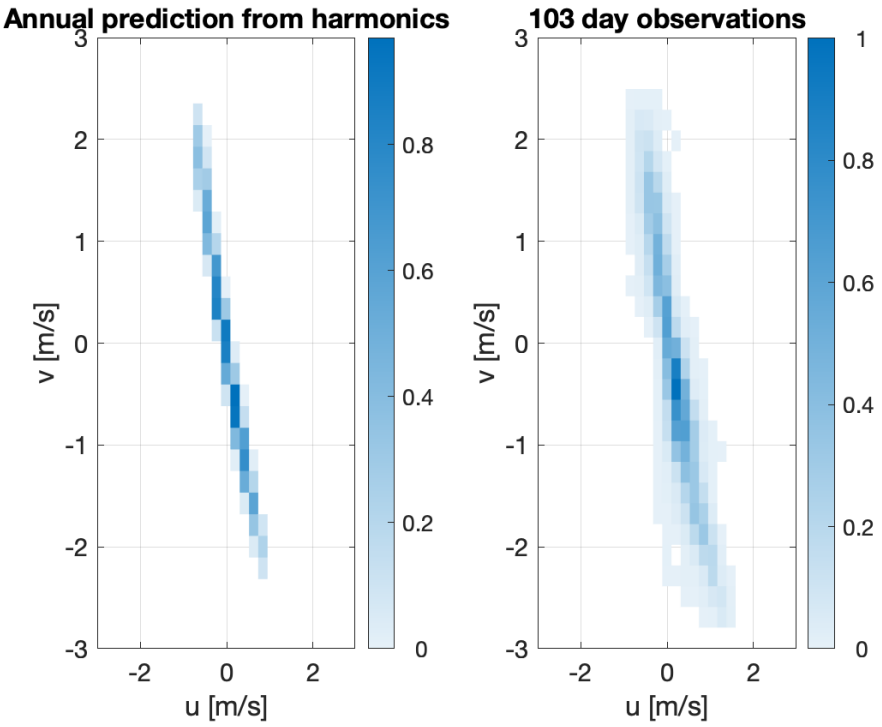

Figure D1: Joint probability of velocity components from harmonic reconstruction (left, 1 year duration) and from observations (right, 103 days duration).

Figure D2 shows the exceedance probability of scalar current speed at hub depth from the harmonic reconstruction and observations. In the region of power production ($U > 1$ m/s), the curves agree well, though the observations have slightly more probability for the highest speeds. The annual prediction has a slight bias towards lower speeds.

When using harmonic reconstruction to produce a full year time series of velocity, the resulting $AEP = 4.1$ GWh is slightly less than the statistical estimate using the direct observations. Based on the work of Polagye and Thomson [2013], we expect the statistical estimate to be a more accurate representation of the site.

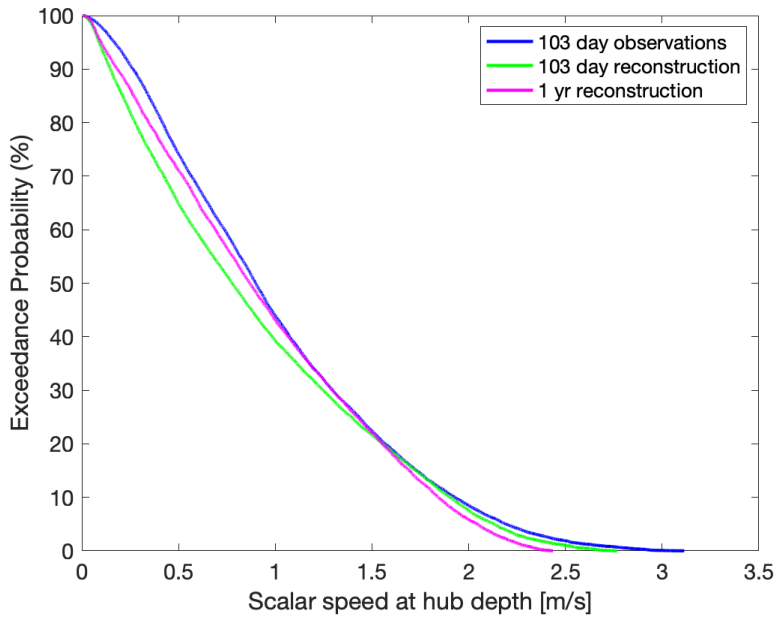

Figure D2: Exceedance probabilities for scalar current speed a hub depth. Results for 103 day observations (blue), 103 day reconstruction (green), and 1 yr reconstruction (magenta).

The full harmonic analysis is given in Table 3, and these values are included in the data submitted to MHKDR. The columns are

- Name of constituent
- Frequency of tidal constituent [cycles/hr]
- Major and Minor axes of constituent [m/s]
- E_{maj}, E_{min} 95% confidence intervals major and minor values
- Inc, ellipse orientations [degrees]
- E_{inc}, 95% confidence intervals for Inc
- Phase of constituent (degrees relative to Greenwich)
- E_{phase}, 95% confidence interval for phase
- SNR, signal to noise ratio

Table 3: Tidal Harmonic Analysis results for Sea Spider Sig 250 velocities at hub depth.

Name	**Freq**	**Major**	E_{maj}	**Minor**	E_{min}	**Inc**	E_{inc}	**Phase**	E_{phase}	**SNR**
*MM	0.0015122	0.048	0.018	0.009	0.02	128.12	19.05	193.61	22.72	7
*MSF	0.0028219	0.079	0.020	-0.013	0.01	117.75	9.53	251.24	14.96	16
ALP1	0.0343966	0.018	0.026	0.002	0.01	110.53	42.62	254.73	71.98	0.46
2Q1	0.0357064	0.013	0.026	-0.009	0.02	112.47	143.59	344.51	173.84	0.26
*Q1	0.0372185	0.054	0.026	0.008	0.01	110.66	13.94	176.19	23.46	4.4
*O1	0.0387307	0.349	0.026	0.033	0.01	105.88	2.00	176.83	3.72	1.8e+02
NO1	0.0402686	0.025	0.026	-0.007	0.01	110.40	26.15	195.97	41.72	0.95
*K1	0.0417807	0.808	0.026	0.014	0.01	108.20	0.92	193.82	1.66	9.6e+02
*J1	0.0432929	0.047	0.026	0.005	0.01	108.48	15.53	238.71	27.56	3.2
*OO1	0.0448308	0.027	0.026	0.007	0.01	109.69	19.05	237.28	31.04	1.1
UPS1	0.0463430	0.008	0.022	0.005	0.02	49.63	128.81	137.32	136.25	0.14
EPS2	0.0761773	0.010	0.018	0.001	0.01	99.58	67.68	133.08	104.66	0.31
*MU2	0.0776895	0.033	0.017	0.024	0.01	114.97	65.72	197.32	71.91	3.8
*N2	0.0789992	0.263	0.017	-0.008	0.01	111.53	2.78	276.19	3.88	2.4e+02
*M2	0.0805114	1.193	0.017	-0.030	0.01	109.90	0.60	311.08	0.86	4.8e+03
*L2	0.0820236	0.071	0.018	-0.002	0.01	93.63	13.26	34.12	21.20	16
*S2	0.0833333	0.332	0.017	-0.009	0.01	111.63	2.11	325.22	2.94	3.8e+02
ETA2	0.0850736	0.017	0.018	0.007	0.01	99.49	32.99	322.46	45.55	0.96
*MO3	0.1192421	0.038	0.008	-0.001	0.01	129.65	11.07	21.41	11.29	20
M3	0.1207671	0.005	0.008	-0.001	0.01	130.51	105.76	134.28	107.49	0.33
*MK3	0.1222921	0.060	0.008	0.001	0.01	125.02	7.26	40.71	7.52	50
*SK3	0.1251141	0.021	0.008	0.000	0.01	139.64	20.52	2.56	20.18	6.5
*MN4	0.1595106	0.014	0.007	-0.009	0.01	128.67	64.99	105.81	62.78	4.4
*M4	0.1610228	0.026	0.008	-0.019	0.01	146.33	43.23	110.48	45.24	12
SN4	0.1623326	0.006	0.008	-0.003	0.01	153.75	78.65	112.90	93.07	0.67
*MS4	0.1638447	0.037	0.007	-0.010	0.01	130.49	12.93	150.15	12.26	29
S4	0.1666667	0.005	0.008	0.000	0.01	167.92	69.74	45.05	100.37	0.33
*2MK5	0.2028035	0.038	0.007	0.006	0.01	120.93	11.18	277.60	10.82	28
2SK5	0.2084474	0.005	0.007	0.002	0.01	136.69	112.64	264.63	112.94	0.43
*2MN6	0.2400221	0.014	0.006	0.005	0.00	173.45	27.60	91.45	32.68	5.8
*M6	0.2415342	0.021	0.006	0.010	0.00	169.11	22.61	95.37	25.77	12
*2MS6	0.2443561	0.023	0.006	0.009	0.00	12.52	16.37	356.89	19.17	15
*2SM6	0.009	0.006	0.000	0.00	20.43	32.41	356.11	38.64	2.4	15
*3MK7	0.2833149	0.011	0.005	-0.004	0.01	66.80	34.44	111.57	32.59	4.8
*M8	0.3220456	0.015	0.004	0.001	0.00	103.77	19.62	221.56	17.71	14
*M10	0.4025570	0.009	0.004	-0.002	0.00	126.24	36.07	48.18	34.98	4.7

E Additional calculations for FERC application

This appendix presents additional calculations required for FERC license application. The FERC Whitepaper for hydrokinetic projects includes several required metrics that are ill-defined for tidal sites, but are still required because the hydrokinetic license application was adapted from conventional hydropower in rivers. The FERC requirements are quoted in italics and answers follow.

The estimated average head on the plant.

The average tidal elevation change of 2.1 m could be used to indicate the average head, though this is physically not the same metric. Operation of the turbines would, for example, not cause this head drop in Rosario Strait across the array.

The estimated minimum and maximum hydraulic capacity of the plant (flow through the plant) in cubic feet per second.

The volumetric flow rate through the swept area of a single turbine would vary from a minimum of 0 cfs to a maximum of 65,584 cfs. The 'plant' has two turbines, so maximum of 131,168 cfs.

The estimated average flow of the stream or water body at the plant or point of diversion.

The average volumetric flow rate through a single turbine would be 20,728 cfs, and thus 41,456 cfs for the two-turbine plant. The average volumetric flow through all of Rosario Strait (i.e., the water body) can be approximated with a tidal prism analysis, which considers the volume of water exchanged with each tide. For Rosario Strait, this has an average value of 289,000 cfs.

Monthly min/max/mean for: Temporal current speed and wave activity

As shown in Figure E1, tidal flows are highly periodic and do not have the strong seasonal variations of a river basin hydrograph. The monthly minimum will always be zero, given the slack tides that occur each day, and the monthly maxima will only vary slightly based on lunar and solar perigee-apogee cycles. The strongest tides (here, 3.2 m/s = 10.6 ft/s) will occur during full and new moons, and during the solistic and equinox. The tidal harmonic analysis in the preceding appendix gives the full annual cycle.

The wave activity is far less regular (see Figure 16), since the waves are generated by local wind and weather patterns. The max observed $H_s = 1.8$ m in December can be considered a global maximum for all months, though the summer months are expected to have far less wave activity. The wave minimum in any month is nominally zero.

Section 5.6(d)(3)(iii)(C) – A monthly water velocity duration curve based on available flow data and the correlation of flow (cubic feet per second) to velocity (feet per second) at the project site.

Tidal channels are not monitored for volumetric flow rates the way rivers are. The flow in Rosario Strait (in cfs or m^3/s) can only be crudely estimated using a tidal prism analysis. Of course, there is a relationship between the volume flow rate of Rosario Strait and the current speed at the site, but it is not an operationally useful metric (nor can it be robustly determined from observations). Such information could be obtained from a numerical model, such as the FVCOM model referenced elsewhere in this report.

An alternative is to present the relation between tidal stage (elevation) and current speed at turbine hub depth. As shown in the right panel of Figure E1, the current speeds are fastest ($\sim$ 3 m/s) at the lowest tidal stage. The apparent 'scatter' in this plot is actually the phasing of tidal stage and tidal flow, which is not 1:1 depending upon spring-neap cycles, diurnal inequalities, and basin geometry. These patterns and distributions are expected to be similar for any other three-month window throughout the year.

Project's dependable capacity.

Tidal flows are highly dependable, since they are based lunar and solar motion, not weather. The predicted capacity factor is $CF \approx 0.20$, based on a rated power of $P = 1.3MW$.

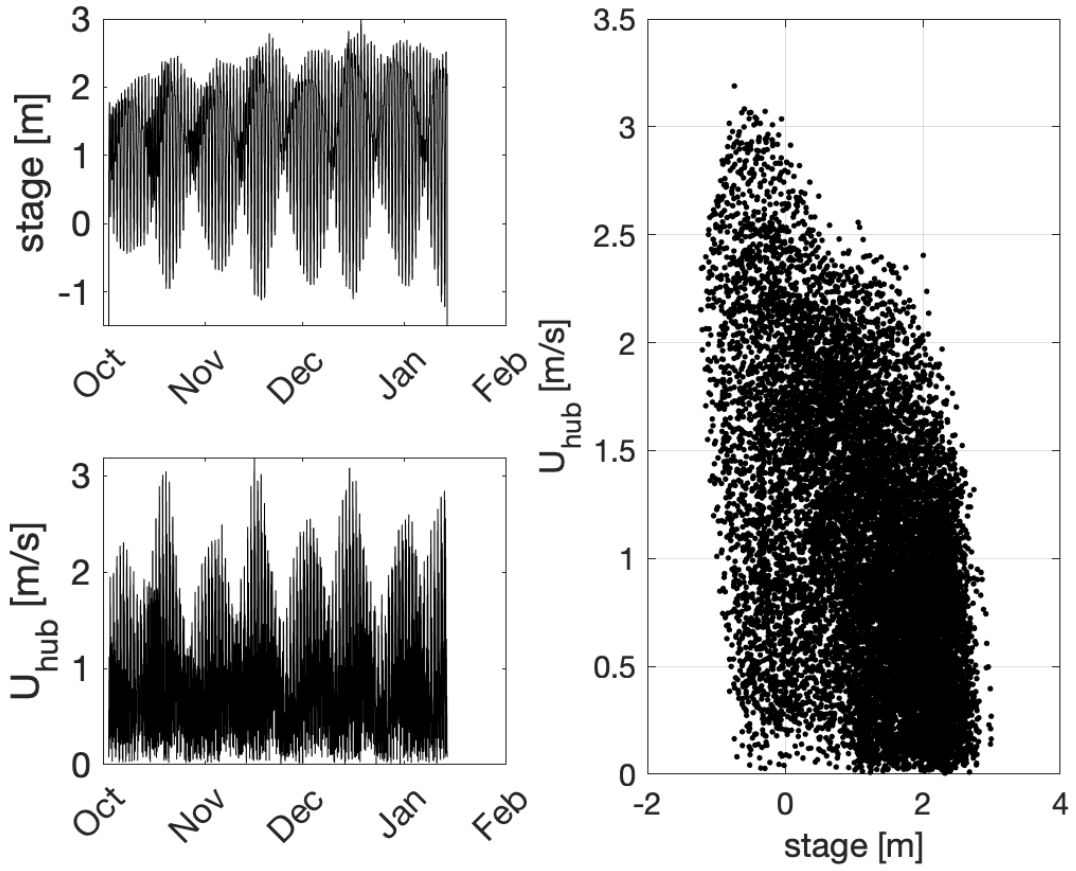

Figure E1: Time series of water depth (upper left) and current speed (lower left). Current speeds versus tidal stage (right).